CONNECTING LAND-ATMOSPHERE INTERACTIONS TO SURFACE HETEROGENEITY IN CHEESEHEAD 2019

Brian J. Butterworth, Ankur R. Desai, Stefan Metzger, Philip A. Townsend, Mark D. Schwartz, Grant W. Petty, Matthias Mauder, Hannes Vogelmann, Christian G. Andresen, Travis J. Augustine, Timothy H. Bertram, William O.J. Brown, Michael Buban, Patricia Clearly, David J. Durden, Christopher R. Florian, Eliceo Ruiz Guzman, Trevor J. Iglinski, Eric L. Kruger, Kathleen Lantz, Temple R. Lee, Tilden P. Meyers, James K. Mineau, Erik R. Olson, Steven P. Oncley, Sreenath Paleri, Rosalyn A. Pertzborn, Claire Pettersen, David M. Plummer, Laura Riihimaki, Joseph Sedlar, Elizabeth N. Smith, Johannes Speidel, Paul C. Stoy, Matthias Sühring, Jonathan E. Thom, David D. Turner, Michael P. Vermeuel, Timothy J. Wagner, Zhien Wang, Luise Wanner, Loren D. White, James M. Wilczak, Daniel B. Wright, Ting Zheng

AFFILIATIONS: Butterworth, Desai, Metzger, Petty, Mineau, and Paleri – Department of Atmospheric and Oceanic Sciences, University of Wisconsin-Madison, Madison, Wisconsin; Townsend, Kruger, and Zheng – Department of Forest and Wildlife Ecology, University of Wisconsin-Madison, Madison, Wisconsin; Metzger, Durden, and Florian – National Ecological Observatory Network Program, Battelle, Boulder, Colorado; Schwartz and Iglinski – Department of Geography, University of Wisconsin-Milwaukee, Milwaukee, Wisconsin; Mauder, Vogelmann, Speidel, and Wanner – Institute of Meteorology and Climate Research - Atmospheric Environmental Research, Karlsruhe Institute of Technology, Garmisch-Partenkirchen, Germany; Andresen – Department of Geography, University of Wisconsin-Madison, Madison, Wisconsin; Augustine – Class ACT Charter School, Chequamegon School District, Park Falls, WI; Bertram and Vermeuel – Department of Chemistry, University of Wisconsin-Madison, Madison, Wisconsin; Brown, Oncley – National Center for Atmospheric Research, Earth Observing Laboratory, Boulder Colorado; Buban and Lee – Cooperative Institute for Mesoscale Meteorological Studies and NOAA Air Resources Laboratory Atmospheric Turbulence and Diffusion Division, Oak Ridge, Tennessee; Clearly – Department of Chemistry and Biochemistry, University of Wisconsin-Eau Claire, Eau Claire, Wisconsin; Lantz, Riihimaki, and Sedlar – Cooperative Institute for Research in Environmental Sciences (CIRES), University of Colorado, Boulder, Colorado and National Oceanic and Atmospheric Administration (NOAA), Boulder, Colorado; Meyers – Atmospheric Turbulence and Diffusion Division, Air Resources Laboratory, National Oceanic and Atmospheric Administration (NOAA), Oak Ridge, Tennessee; Olson, Pettersen, Thom, and Wagner – Space Science and Engineering Center (SSEC), University of Wisconsin-Madison, Madison, Wisconsin; Pertzborn – Center for Climate Research, Nelson Institute for Environmental Studies, UW-Madison, Madison, Wisconsin; Plummer – Department of Atmospheric Science, University of Wyoming, Laramie, Wyoming; Guzman – Department of Forest Production, University of Guadalajara, Guadalajara, Jalisco, Mexico; Smith – National Severe Storms Laboratory, National Oceanic and Atmospheric Administration (NOAA), Norman, Oklahoma; Stoy – Department of

Biological Systems Engineering, University of Wisconsin–Madison, Madison, Wisconsin; SÜHRING – Institute of Meteorology and Climatology, Leibniz University of Hannover, Germany; TURNER – Global Systems Laboratory, National Oceanic and Atmospheric Administration (NOAA), Boulder, Colorado; WANG – Laboratory for Atmospheric and Space Physics and Department of Atmospheric and Oceanic Sciences, University of Colorado Boulder, Boulder, Colorado; WHITE – Department of Chemistry, Physics, and Atmospheric Science, Jackson State University, Jackson, Mississippi; WILCZAK – Physical Sciences Laboratory, National Oceanic and Atmospheric Administration (NOAA), Boulder, Colorado; WRIGHT – Civil and Environmental Engineering, University of Wisconsin-Madison, Madison, Wisconsin

CORRESPONDING AUTHOR: Brian J. Butterworth, bbutterworth@wisc.edu

ABSTRACT

The Chequamegon Heterogeneous Ecosystem Energy-balance Study Enabled by a High-density Extensive Array of Detectors 2019 (CHEESEHEAD19) is an ongoing National Science Foundation project based on an intensive field campaign that occurred from June-October 2019. The purpose of the study is to examine how the atmospheric boundary layer responds to spatial heterogeneity in surface energy fluxes. One of the main objectives is to test whether lack of energy balance closure measured by eddy covariance (EC) towers is related to mesoscale atmospheric processes. Finally, the project evaluates data-driven methods for scaling surface energy fluxes, with the aim to improve model-data comparison and integration.

To address these questions, an extensive suite of ground, tower, profiling, and airborne instrumentation was deployed over a 10×10 km domain of a heterogeneous forest ecosystem in the Chequamegon-Nicolet National Forest in northern Wisconsin USA, centered on the existing Park Falls 447-m tower that anchors an Ameriflux/NOAA supersite (US-PFa / WLEF). The project deployed one of the world's highest-density networks of above-canopy EC measurements of surface energy fluxes. This tower EC network was coupled with spatial measurements of EC fluxes from aircraft, maps of leaf and canopy properties derived from airborne spectroscopy, ground-based measurements of plant productivity, phenology, and physiology, and atmospheric profiles of wind, water vapor, and temperature using radar, sodar, lidar, microwave radiometers, infrared interferometers, and radiosondes. These observations are being used with large eddy simulation and scaling experiments to better understand sub-mesoscale processes and improve formulations of sub-grid scale processes in numerical weather and climate models.

CAPSULE SUMMARY

A regional-scale observational experiment designed to address how the atmospheric boundary layer responds to spatial heterogeneity in surface energy fluxes.

INTRODUCTION

Land-atmosphere exchanges of energy, water, and carbon influence weather and climate. The biological processes that mediate these exchanges with the atmosphere occur at multiple spatial and temporal scales, necessitating a variety of cross-scale observational platforms. Accurate accounting of land-atmosphere interactions is critical for improving the predictive performance of numerical weather and climate models. Unfortunately, there is a persistent mismatch between the scales of observations and models. This scale mismatch is problematic because natural environments exhibit substantial heterogeneity in their surface characteristics, which means that observations are not always accurate reflections of the entire model grid cell. Furthermore, the atmosphere is strongly influenced by nonlinear two-way interactions with radiation, land cover, and soil, so that the spatial and temporal scaling of surface fluxes is fundamental to assessing the parameterizations used in atmospheric models to represent land-atmospheric interactions.

The notion that land surface heterogeneity influences the surface energy balance, and the resulting atmospheric responses, emerged from early model simulations showing the importance of soil moisture, vegetation, albedo, roughness, and heating on the atmosphere (Garratt 1993; Mahrt 2000; Betts et al. 1996; Charney 1975; Avissar 1995; Pielke et al. 1998). Theories on how land surface variations drive atmospheric boundary layer (ABL) growth vary (e.g., Desai et al. 2006; Reen et al. 2014; Platis et al. 2017; Gantner et al. 2017), with no consensus on whether responses scale linearly or non-linearly and whether they differ for dry versus moist dynamics (Raupach and Finnigan 1995). Modeling studies on this topic have been developed from limited sets of observations of prior field experiments and from specialized modeling domains using simplified boundary conditions (e.g., Kang et al., 2007; Hill et al., 2008, 2011; Zhu et al., 2016). From these previous studies, scaling laws have been derived based on numerical simulations (van Heerwaarden et al. 2014; Rihani et al. 2015), but a systematic regional-scale observational experiment that quantifies the multi-scale nature of sub-grid scaling and patterning has never been fully realized (Steinfeld et al. 2007).

An issue related to how heterogeneity influences transport processes in the ABL is the energy balance closure problem. This refers to an observed tendency in eddy covariance (EC) flux measurements, where the sum of incoming available energy (net radiation [R_N] minus ground heat flux [G]) exceeds surface turbulent sensible and latent heat fluxes (H_S and H_L) over sub-hourly time scales (Foken et al. 2011). Systematic studies have ruled out instrument errors as the primary cause (Twine et al. 2000; Frank et al. 2013; Liu et al. 2011). Incomplete observation of sub-measurement height storage flux accounts for only some of this lack of closure (Leuning et al. 2012; Xu et al. 2018). Advection terms are not expected to have a systematic direction that would always lead to lack of closure (e.g., Aubinet et al. 2010; Barr et al. 2013; Nakai et al. 2014; Zitouna-Chebbi et al. 2012), while topography contributes mostly in extreme cases (Mcgloin et al. 2018).

EC sites with more variable land cover tend to have larger closure imbalances (Stoy et al. 2013; Xu et al. 2017b). One proposed hypothesis for lack of closure in the energy budget is that surface heterogeneity generates mesoscale features not adequately resolved by traditional EC methods (e.g., Charuchittipan et al. 2014; Gao et al. 2016; Foken et al. 2011; Mauder et al. 2007b). An intensive suite of energy flux measurements between surface and atmosphere at the mesoscale (on the order of tens of kilometers) can help address this key uncertainty in land-atmosphere exchange (Xu et al. 2020).

EXPERIMENTAL GOALS

CHEESEHEAD19 was designed to provide a new level of observation density and instrumentation reliability to test hypotheses on spatial heterogeneity and atmospheric feedbacks. The two main research objectives for the CHEESEHEAD19 experiment were to 1) investigate causes of energy balance non-closure over heterogeneous ecosystems and 2) to address the problem of scaling surface energy fluxes.

There is currently no definitive answer as to what is responsible for energy balance non-closure. The project was designed specifically to test the hypothesis that heterogeneity is responsible for generating organized (sub-)mesoscale structures that are not resolved by traditional EC methods.

Various theories suggest that "spatial" EC, where multiple towers are combined to estimate the mesoscale contribution to the total flux, could be used to analyze this contribution and "close" the energy balance (Steinfeld et al. 2007; Mauder et al. 2008b). To calculate spatial fluxes, CHEESEHEAD19 deployed an EC tower network and airborne EC measurements. These measurements provide spatial patterns of surface energy fluxes across various vegetation and surface types in the heterogeneous landscape. Alongside this EC flux network, multiple platforms were deployed to characterize the atmospheric environment by profiling relevant atmospheric characteristics across a range of scales. This allows us to determine the existence and to characterize the nature of organized mesoscale structures. We can investigate the degree to which mesoscale eddies are responsible for energy balance non-closure in EC measurements, and whether land surface energy partitioning and atmospheric responses differ from the sum of their individual components.

To systematically address surface energy balance variability in the heterogeneous forested landscape, a pre-campaign large eddy simulation (LES) analysis of the study domain was conducted. It was found that, while 12 flux towers would be sufficient to adequately sample land cover variation, >15 flux towers are required to sample mesoscale eddy structures and close the energy budget (a similar result to Steinfeld et al., 2007). Therefore, the CHEESEHEAD19 field campaign deployed 20 flux towers, a marked increase over many previous experiments.

CHEESEHEAD19 asks how we can optimally observe and simulate the terms of the surface energy balance and the corresponding atmospheric responses to heterogeneous surface forcings. The objective is to evaluate methods for scaling surface energy fluxes, with the aim of improving model-data comparisons. To this end, we conduct LES and machine-learning scaling experiments to simulate sub-mesoscale responses. These will be compared to measured quantities to test existing theoretical concepts and to improve our understanding of how scale-dependent transport processes in the lower atmosphere respond to surface heterogeneity. The dataset collected during this study will help test multiple scaling methodologies across heterogeneous land cover. Specifically, it aims to test the *environmental response function - virtual control volume* (ERF-VCV) approach (Metzger 2018; Xu et al. 2018), which combines the strengths of both data-driven and mechanistic strategies.

Several additional research objectives are addressed by using the unique data resources of CHEESEHEAD19. These include a separately funded study to use CO_2 fluxes of Integrated Surface Flux System (ISFS) towers and hyperspectral imagery of canopy functional traits to determine the principal drivers of variation in NPP and carbon use efficiency across a broad array of forest ecosystems. Additionally, concurrent measurements of ozone (O_3) mixing ratios at 30- and 122-m on the tall tower were made using a chemical ionization time-of-flight mass spectrometer (CI-ToFMS; TOFWERK AG and Aerodyne Research Inc.) and a photometric analyzer (Model 49i; Thermo Fisher) to obtain vertical O_3 profiles above the forest canopy

(Bertram et al. 2011; Novak et al. 2020). These measurements were accompanied by flights of a sUAS-mounted lightweight O_3 monitor (POM; 2B) that obtained vertical concentration gradients. These measurements are being used to determine the relative contributions of stomatal uptake and other nonstomatal loss pathways to O_3 deposition within a mixed forest canopy.

THE EXPERIMENT

Overview

CHEESEHEAD19 investigators deployed an extensive suite of ground, tower, profiling, and airborne instrumentation over a 10 × 10 km domain in a forested and aquatic landscape in northern Wisconsin USA (Fig. 1; Table 1), centered on the existing Park Falls 447-m tower Ameriflux/NOAA supersite (US-PFa / WLEF). The main components of the CHEESEHEAD19 field campaign were:

a) ground-based fluxes and meteorology
b) airborne fluxes and meteorology
c) atmospheric profiling
d) surface environment characterization

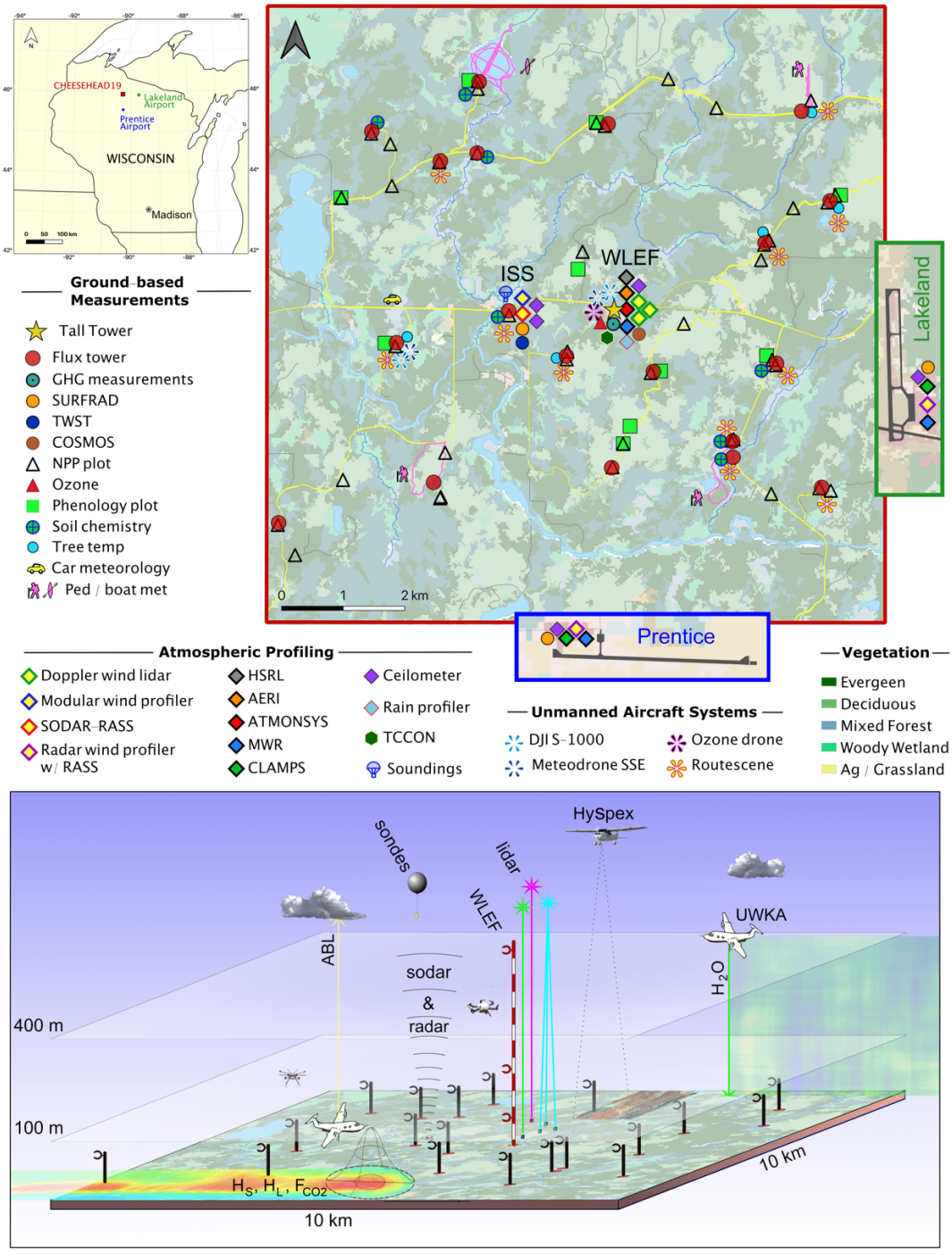

Fig. 1. Map and schematic diagram of CHEESEHEAD19 domain. Map shows the location of all measurements made during the field campaign. Insets show Lakeland and Prentice airports where SURFRAD (in addition to the one in ISS field), radar wind profilers with RASS, and CLAMPS systems were installed. Schematic diagram shows instrument location and a conceptual model of airborne data collection. (Wisconsin Department of Natural Resources 2019)

The EC tower network consisted of 17 towers from the NSF Lower Atmosphere Observing Facility (LAOF) ISFS, two additional towers, and the central tall Ameriflux tower. Ground-based measurement of vegetation occurred at 41 plots in the domain, plus an additional 10 plots for measuring phenology. Airborne spectroscopy imaging was used to map leaf chemistry and canopy properties.

The suite of atmospheric profiling instruments included the LAOF Integrated Sounding System (ISS; Fig. 2c) and the UW SPARC system (Fig. 2a). Additional instrument systems were brought by collaborators, including the combined ATMONSYS lidar for measuring aerosol, T, and H_2O profiles and two Doppler wind lidars brought by Karlsruhe Institute of Technology (KIT), two Collaborative Lower Atmospheric Profiling Systems (CLAMPS – NOAA NSSL), two 915 MHz radar wind profilers with radio acoustic sounding systems (RASS) with MWRs (NOAA PSL), and the Surface Radiation Budget Network (SURFRAD – NOAA GML) systems for measuring incoming and outgoing radiation and cloud properties. While many of these instruments were located within the 10 ×10 km CHEESEHEAD19 domain, some instruments were located at the Prentice and Lakeland airports, located approximately 45 km south and east of the WLEF tower respectively, to provide information on the spatial variability of boundary layer structure and cloud and radiation fields.

Three seven-day intensive observation periods (IOP) occurred on July 7 – 13, August 18 – 24, and September 22 – 28. During these IOPs the University of Wyoming King Air (UWKA) flew transects over an extended 30 × 30 km domain to measure EC fluxes, ABL depth, and atmospheric profiles of water vapor and temperature. These observations will be used to test flux tower scaling, observe atmospheric mesoscale patterning, and evaluate large eddy simulations (LES). Also, during the IOPs, a team from NOAA ARL ATDD brought multiple sUASs for measuring profiles of meteorological variables (T, H_2O, U, P – see appendix for a list of variables used in this paper) and land surface temperature. Additional information on the spatial variations of surface meteorology was obtained using mobile observing systems operated in pedestrian, boat, and car modes.

The four-month deployment spanned the summer to fall transition, capturing the shift in surface energy balance from a more uniform evapotranspiration (latent heat flux) dominated landscape to a patchy sensible heat flux dominated landscape. These energy balance shifts arise from seasonal changes in plant phenological phases, ecosystem water use for photosynthesis, and available net radiation. These shifts also provide a "natural experiment" with which to test hypotheses on how heterogeneity influences energy balance closure and spatial scaling.

The study domain was partly chosen due to the history of atmospheric science research in the region. Since 1995, University and NOAA investigators have sampled greenhouse gas profiles, meteorology, and EC flux measurements (energy, carbon, momentum) at 30 m, 122 m, and 396 m above ground level (AGL; Fig. 2b) on the WLEF tall tower (Bakwin et al. 1998; Davis et al. 2003). The site also includes an FTIR solar-pointing spectrometer (TCCON) for total greenhouse column observations operated by CalTech and NASA JPL. Two additional EC towers (US-WCr,

30 m in mature forest, and US-Los, 10 m in shrub fen wetland) have been operating for 20 years, approximately 20 km from the tall tower (Cook et al. 2004; Desai et al. 2005; Sulman et al. 2009).

CHEESEHEAD19 builds upon previous tower mesonet experiments, including BOREAS (Sellers et al. 1995), CASES99 (Poulos et al. 2002), SGP97 (Desai et al. 2006), IHOP (Kang et al. 2007), LITFASS-2003 (Beyrich et al. 2006), EBEX (Oncley et al. 2007), BEAREX (Anderson et al. 2012), HiWATER-MUSOEXE (Wang et al. 2015), SCALE-X (Wolf et al. 2017), that were aimed at understanding scaling of non-linear land-atmosphere interaction.

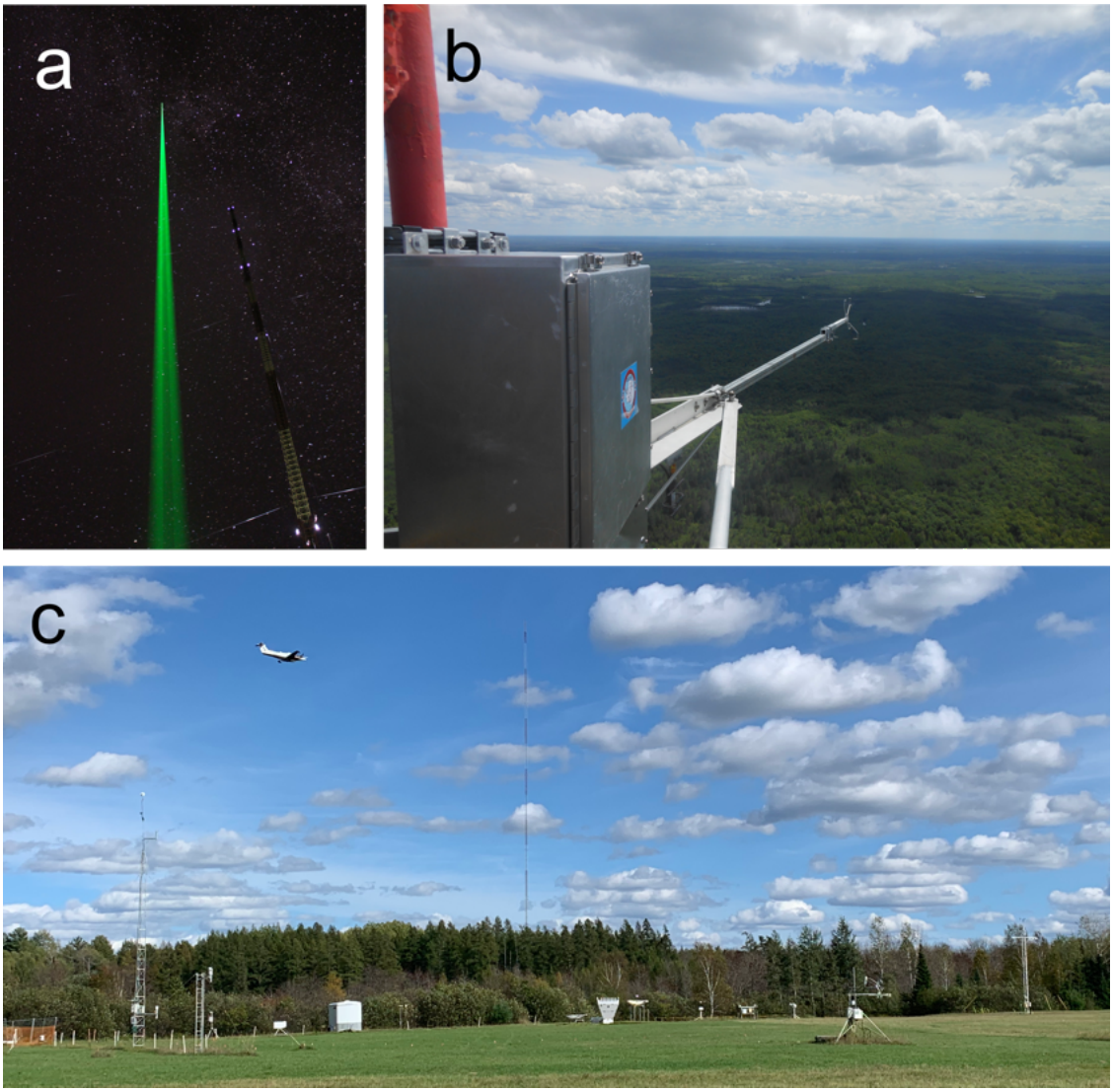

Fig. 2. (a) HSRL beam next to WLEF tall tower, (b) EC instruments at 396 m AGL on the WLEF tall tower, and (c) the ISS field with modular wind profiler, sodar-RASS, ceilometer, SURFRAD, EC and meteorological towers with UWKA flying overhead and WLEF tall tower in the distance.

Table 1. List of instruments and data collected during CHEESEHEAD19. For explanation of the variable abbreviations please see the appendix.

Data source	Data provider	Location(s)	Measured Variables	Period
Ground-based Measurements				
Ameriflux/NOAA tall tower (US-PFa/WLEF)	UW AOS	WLEF	H_S, H_L, F_{CO2}, τ, R_n, meteorology	Continuous
ChEAS Ameriflux towers: US-WCr / US-Los / US-Syv / US-Alq	UW AOS	Ameriflux sites (4)	H_S, H_L, F_{CO2}, τ, R_n, meteorology	Continuous
ISFS Eddy covariance towers	NCAR EOL ISFS	10x10 km (17 sites)	H_S, H_L, F_{CO2}, τ, R_n, meteorology, soil G, Q, Cv, T profile, precip (5 sites)	June-Oct
MSU Eddy covariance towers	Montana State U & UW BSE	NW5 (ISS) and SE1	H_S, H_L, F_{CO2}, τ, R_n, soil G, meteorology	June-Oct
Surface meteorology	NCAR EOL ISS	ISS field	T, RH, P, precip, wind, sky images	July-Oct
SURFRAD & TWST	NOAA GML	ISS field[1] Prentice Airport[2] Lakeland Airport[2]	Downwelling SW/LW[1,2], direct SW[1,2], diffuse SW[1,2], upwelling SW/LW[1], PAR[1], sky images[1], cloud optical depth[1], cloud fraction[1,2], cloud base height[2], mixed layer depth[2], meteorology[1]	July-Oct (TWST: Sep-Oct)
Vehicle/ Pedestrian/ Boat transects	Jackson State U	10x10 km – Roads/ Trails / Hay Lake	T, RH, P, total downwelling SW, IR brightness temperature, water T	IOP 1, 2, 3
Chemical ionization mass spec & ozone photometric analyzer	UW Chem	WLEF	Ozone concentration and flux	IOP 1
Tall tower greenhouse gases	NOAA GML	WLEF	CO2, CH4 concentration & CO2, CH4 profiles	Continuous & Biweekly
Tree temperature	Chequamegon HS	5 sites, 10 trees	T at breast height (1.37 m AGL)	Oct
Atmospheric Profiling				
449 MHz modular wind profiler	NCAR EOL ISS	ISS field	3D wind profiles	July-Oct
Sodar / RASS	NCAR EOL ISS	ISS field	3D wind, T_v and θ_v profiles	July-Oct
Ceilometer	NCAR EOL ISS	ISS field	Attenuated backscatter profiles, cloud base height, ABL height	July-Oct
Daily radiosonde	NCAR EOL ISS	ISS field	18Z (1pm local)	July-Oct
3-hourly daytime radiosondes	NCAR EOL ISS	ISS field	4-5 per day for 5 days per IOP	IOP 1, 2, 3
AERI	UW SSEC SPARC	WLEF	Downwelling IR radiance, profiles of T, H_2O, and cloud properties	July-Oct
HALO Lidar (1) – vertical stare	UW SSEC SPARC	WLEF	Profiles of 3D wind (virtual tower)	July-Oct
HSRL	UW SSEC SPARC	WLEF	Backscatter, depolarization	July-Oct
Micro Rain Radar (MRR)	UW SSEC	WLEF	Precipitation rate, reflectivity, particle size distribution (PSD)	July-Oct
Precipitation Imaging Package	UW SSEC	WLEF	PSD, fall speed, rain rate	July-Oct
ATMONSYS: Backscatter, Raman, and Differential Absorption Lidar	KIT IMK-IFU	WLEF	Vertical profiles of aerosol backscatter, T, H_2O	July-Sep
HALO Lidars (2,3) – RHI scans	KIT IMK-IFU	WLEF	Profiles of 3D wind (virtual tower)	July-Sep
915 MHz radar wind profiler w/ radio acoustic sounding system	NOAA PSL	Prentice Airport, Lakeland Airport	Profiles of U, T_v, Convective ABL height	July-Oct
MWR	NOAA PSL	ISS field[1] Prentice Airport[2] Lakeland Airport[3]	Downwelling microwave radiance, profiles of T, H_2O, and liquid water path	July-Oct[3] July-Sep[2] Sep-Oct[1]
CLAMPS (MWR, AERI, Doppler wind lidar)	NOAA NSSL	Prentice Airport, Lakeland Airport	Profiles of U, T, H_2O	Sep-Oct
Airborne Measurements				
Airborne eddy covariance	UWKA	30x30km, 24 flights	3D wind, T, H2O, CO2 (25 Hz; ~3 m)	IOP 1, 2, 3
Airborne met. and radiation	UWKA	30x30km, 24 flights	Meteorology (1 Hz; ~80 m)	IOP 1, 2, 3

Compact Raman Lidar (CRL)	UWKA	30x30km, 24 flights	H2O and T cross sections	IOP 1, 2, 3
Wyoming Cloud Lidar (WCL)	UWKA	30x30km, 24 flights	ABL height	IOP 1, 2, 3
Meteodrone SSE sUAS	NOAA ARL ATDD	WLEF and SW2	T, H2O, U	IOP 1, 2, 3
Ozone sUAS	UWEC	WLEF	O_3 profiles	IOP 1
Surface Environment				
HySpex	UW FWE	10x10 km, 4 flights	hyperspectral imagery (474 bands), foliar functional traits	June-Aug
DJI S-1000 (sUAS)	NOAA ARL ATDD	WLEF and SW2	LST, Hs	IOP 1, 2
sUAS leaf-on canopy LiDAR	UW Geog	11 tower sites	Ground and canopy height	June
QL2 leaf-off LiDAR	USFS	30x30 km	Ground and canopy height	Fall 2018
Vegetation/phenology sampling	UWM Geog	10x10 km (10 plots)	Leaf color / fall level	Sep-Oct
Vegetation Sampling	UW FWE	10x10 km (41 plots)	inventory, root growth, NPP, biometry, leaf spectra, foliar tissue chemistry, LMA	June-Oct
Soil bulk density and heat capacity	NCAR EOL	17 tower sites	Q_{soil}, ρ_{soil}	July-Oct
Soil samples	UW AOS	16 tower sites	Soil carbon, nitrogen	Oct
Soil samples	Butternut Schools	7 sites	Soil and water chemistry	July
ECOSTRESS, GEDI, OCO3	NASA JPL	30x30 km	LST, emissivity, evapotranspiration	Oct 8

Ground-based Measurements

Towers sampled three-dimensional wind velocity, temperature, moisture, and CO_2 at 20 Hz to measure land-atmosphere fluxes (τ, H_S, H_L, F_{CO2}). Each tower also measured net radiation, soil heat flux at 5 cm depth (and soil temperature profile, heat capacity, and moisture to determine soil heat storage), and a 3-level air temperature and humidity profile to estimate canopy heat storage. A majority of the sites were forested and had flux instruments mounted 33 m AGL (Fig. 3; Table S1). Instruments for wetland, grass, and lake sites were mounted between 1 – 3 m AGL to maintain consistent vegetation within the flux footprint. Tower placement within the 10 × 10 km study domain followed a stratified random grid pattern, taking into account practical considerations including distance to road, suitable gap in trees for a tower, USFS-owned land, etc. Individual towers were an average of 1.4 km from their nearest neighboring tower and an average of 3.5 km from the tall tower. This meant that under certain conditions (e.g., high wind speeds, stable stratification) several of the towers shared overlapping flux footprints; a favorable condition for applying some of the data-driven scaling methods used in the project. Additionally, the semi-random placement meant that the towers were not chosen by distributing the towers in the centers of the most homogeneous areas of the various land cover types. Thus, within the individual footprint of each tower there was often spatial variability in vegetation height and type (deciduous vs. evergreen). While this can complicate analyses of flux measurements, it generates more representative data from these types of mixed forests. Furthermore, we expect it will enhance the ability of the data-driven methods for estimating domain-wide fluxes.

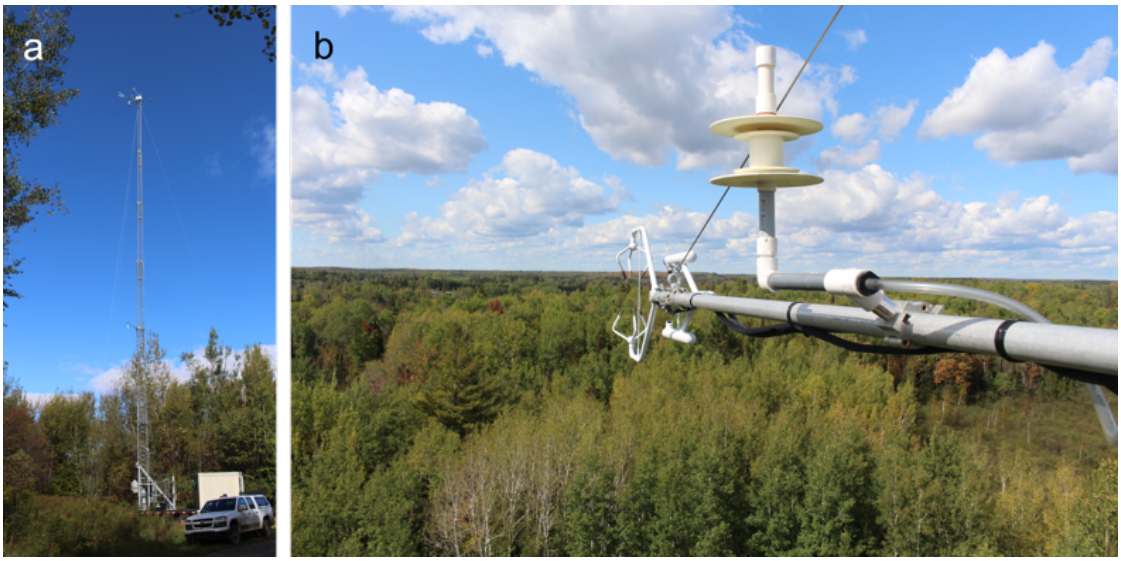

Fig. 3. (a) EC tower SW1 – an example of the 33 m AGL telescoping towers deployed by NCAR ISFS and (b) EC instruments mounted at the top of tower SW2.

A suite of high-quality radiation sensors was deployed in the ISS field as a complement to the net radiometers installed on each flux tower. The full suite included high-quality upwelling and downwelling broadband surface radiation measurements to determine the surface radiation budget, as well as ancillary measurements of meteorological parameters, photosynthetically active radiation (PAR), and clouds as described in Table S2. Radiation measurements are manually screened and then processed through an automated data quality procedure (Long and Shi 2008). Clear sky radiation fluxes are estimated using the Radiative Flux Analysis method (Long and Ackerman 2000; Long and Turner 2008), from which derivation of cloud radiative effects as well as other data products such as fractional sky cover (Long et al. 2006; Dürr and Philipona 2004) and cloud optical depth (Barnard and Long 2004; Niple et al. 2016) are calculated. Measurements of cloud properties will allow us to quantify their impacts on the radiative and turbulent heat fluxes to better understand the two-way coupling between cloud-radiative interactions and boundary layer evolution, and to investigate the effect on EC non-closure.

A smaller suite of radiation, cloud, and surface meteorological measurements were deployed at the Prentice and Lakeland Airports, approximately 45 km south and east from the ISS field, respectively (Fig. 1), to characterize the larger spatial scale inhomogeneities. These measurements include downwelling shortwave and longwave irradiance as well as diffuse and direct components of shortwave irradiance (Table S2); sufficient information to derive cloud radiative effects and fractional sky cover using the Radiative Flux Analysis method described above. Ceilometers deployed at the two airport sites provided additional cloud and boundary layer information.

Airborne Measurements

During each IOP the UWKA flew over the study area to measure spatial EC fluxes of heat, water vapor, and CO_2. The purpose of the observations was to test flux tower scaling and observe atmospheric mesoscale patterning. The UWKA also measured cross-sectional profiles of water vapor and temperature below the flight level using a downward pointing Compact Raman Lidar (CRL, Wu et al. 2016) and ABL depth with the upward looking Wyoming Cloud Lidar (WCL, Wang et al. 2009).

Flights over the domain occurred on four days during each of the three IOPs (Table S3). On each day there were two three-hour flights, one in the morning (1400 – 1700 UTC) and one in the afternoon (1900 – 2200 UTC). Flights consisted of ten 30-km down-and-back transects across the domain. The first leg of each transect was flown at 400 m AGL, while the return leg was flown at 100 m AGL. Flight transects alternated between straight and diagonal passes.

Three different flight patterns were determined prior to the experiment (oriented SE→NW, SW→NE, and W→E). Flying them either in forward or reverse order resulted in six distinct flight sequences that maximize data coverage under different wind conditions (see sidebar *Continuity through Environmental Response Functions*). The main objectives were to maximize 1) the number of independent atmospheric eddies and 2) surface flux footprint observed by the aircraft EC measurements, while 3) ensuring crew safety. This was achieved by designing a parsimonious set of only three flight patterns that allowed the UWKA to fly perpendicular to the prevailing winds within a range of ±45° on any given day (Metzger et al., in preparation). The 30-km flight legs extended an average of 10 km beyond the domain to compute a robust mesoscale eddy flux (Mauder et al. 2007a, 2008a) by capturing enough eddies and mesoscale variation to properly compute statistics for fluxes using the wavelet decomposition method.

The low-altitude legs were primarily used to measure EC fluxes. The altitude 100 m AGL was chosen to ensure flux measurements were made in the surface layer, as well as to minimize flux footprint errors over the 10 × 10 km sampling domain. It was also the lowest altitude deemed safe to fly, as canopy height extended up to 35 m. The low-altitude legs were also used to identify ABL depth with the upward pointing 355 nm WCL. The primary purpose of the high-altitude legs (400 m AGL) was to map temperature and moisture profiles of the atmosphere with the CRL. These data were collected to estimate mesoscale development and calculate flux divergence and storage terms.

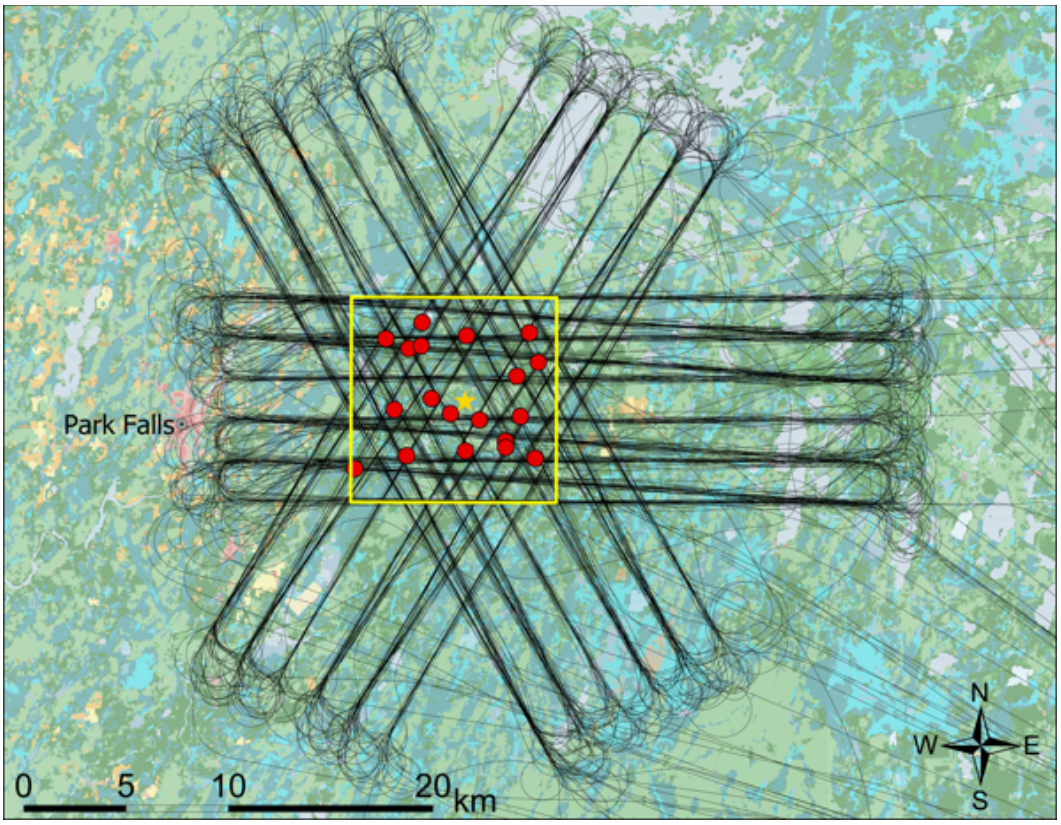

Fig. 4. The location (superimposed) of all 480 flight legs completed during the CHEESEHEAD19 field campaign. The yellow square represents the study domain and the red dots indicate the flux tower locations.

Atmospheric Profiling

Characterizing the mesoscale environment over the study domain was accomplished with a range of platforms and instruments to measure profiles of wind, water vapor, temperature, aerosols, and gases at different temporal and spatial scales (Fig. 1; Table 1).

The NCAR ISS was located in a field 1.6 km west of the tall tower (45.946°N, 90.294°W). It deployed a radar wind profiler, sodar-RASS, ceilometer, all-sky camera, and a surface meteorology station to measure ABL depth, winds, water vapor, and temperature. The 449 MHz modular wind profiler measured 30-minute wind profiles with 150 m vertical resolution up to several km AGL, while the sodar-RASS was capable of higher resolution (20 m; 10-minute), but only penetrated to ~400 m AGL. Meteorological profiles were also measured with 172 radiosonde launches (daily 18Z soundings and 3 – 4 additional soundings on IOP days). These instruments characterized the ABL from nocturnal boundary layer (sunrise sounding), through ABL development (mid-morning and afternoon), to peak ABL (late afternoon sounding). In mid-September, one of the MWRs located at the Prentice Airport was relocated to this location, due to the failure of the AERI at the tall tower site in early September.

Several profiling systems were deployed at the base of the tall tower. SPARC (Wagner et al. 2019) was located 50 m north of the WLEF tower and was equipped with an Atmospheric Emitted Radiance Interferometer (AERI, a zenith-pointing infrared radiometer [Knuteson et al. 2004]), a High-Spectral Resolution Lidar (HSRL [Eloranta 2005]), and a ceilometer. Profiles of boundary layer temperature and humidity were retrieved from the AERI radiance observations (Turner and Löhnert 2014; Turner and Blumberg 2019). The HSRL sampled ABL aerosol backscatter and depolarization ratio at 532 nm and 1064 nm. The ceilometer provided an additional measure of ABL depth.

The ATMONSYS system was placed beside the SPARC system, measuring atmospheric water vapor, temperature, and aerosol. The primary light source of the ATMONSYS lidar is a 100 Hz diode pumped Nd:Yag laser with the harmonic generation of 532 nm and 355 nm. The 532 nm light ($P \simeq 27$ W) is used for optical pumping a Ti:Sapphire laser, generating 817 nm ($P \simeq 2$ W) for water vapor profiling with the high resolving DIAL (Differential Absorption Lidar) method as well as for profiling aerosol backscatter. The 355 nm light is used for temperature profiling from rotational Raman backscatter. The system setup as installed during CHEESEHEAD19 (Vogelmann et al. 2020) allows for spatial sampling of 7.5 m and integration times of 20 s for aerosols and water vapor measurements and 300 s for temperature profiling.

In the field to the east of the trailers were three Doppler wind lidars. One lidar (LVS) measured in vertical stare mode throughout the measurement campaign. The other two lidars (LA, LB) were placed 90 meters away from the LVS and made range–height indicator (RHI) scans (66º – 87º elevation angle) pointing towards the LVS. This setup constitutes a virtual tower that provides vertical wind speed measurements and calculates average horizontal wind speed at multiple height levels above the LVS (Calhoun et al. 2006; Klein et al. 2015; Wulfmeyer et al. 2018). Additionally, the collocation of lidars for measuring 3D winds, temperature, and water vapor facilitates calculation of flux profiles of τ, H_S, and H_L, as well as flux divergence (Wulfmeyer et al. 2016).

Two precipitation instruments (a Precipitation Imaging Package [PIP] and a Micro Rain Radar Pro [MRRPro; Metek GmbH]) were installed at WLEF. The PIP is a video disdrometer system that records information about hydrometers and produces end user products such as particle size distributions, fall speeds, and rain rate at one-minute resolution (Newman et al., 2009; Pettersen et al., 2020a; Pettersen et al., 2020b). The MRRPro is a 24-GHz, frequency modulated continuous wave, vertically profiling Doppler radar (Klugmann et al. 1996) that is used for observations of both rain (i.e., Peters et al. 2002) and snow (Kneifel et al. 2011).

Additional thermodynamic profiling systems were operated at the Prentice and Lakeland airports throughout the experiment to characterize the boundary layer variability and evolution around the CHEESEHEAD19 domain. The primary motivation of these two profiling sites was to characterize the mesoscale transport and role of advection on the ABL mass balance of the CHEESEHEAD19 domain. At each location, a 915 MHz wind profiler with radio acoustic sounding system was deployed together with a multi-channel MWR. These instruments

provided profiles of horizontal wind and temperature, and low vertical resolution profiles of water vapor.

Prior to IOP3, two mobile CLAMPS facilities (Wagner et al. 2019) were deployed at Prentice and Lakeland. The systems contained a Doppler lidar wind profiler, an AERI, and a microwave radiometer (MWR). The information content in the AERI observations is higher than in the MWR, and thus the retrieved water vapor and temperature profiles have better vertical resolution and accuracy (Löhnert et al 2009; Blumberg et al. 2015). The Doppler lidars complemented the radar wind profilers by providing higher temporal and vertical resolution measurements than the radars, but the radars were able to profile winds several km higher than the lidars.

Two small unoccupied aircraft systems (sUAS) were flown to characterize surface and near-surface conditions (Fig. S1). During IOP1 (IOP2), a DJI S-1000 (e.g., Lee et al. 2019) was flown adjacent to the SW2 tower (WLEF tall tower) to quantify the variability in surface sensible heat flux (e.g., Lee et al. 2017). During all three IOPs, the Meteomatics Meteodrone SSE sUAS was used to sample the evolution of near-surface profiles of temperature, moisture, and wind up to 213 m AGL, which was the maximum altitude to which we could operate our sUAS per our cooperative agreement with the FAA. Additionally, the Meteodrone SSE was used to sample the horizontal variability in temperature, moisture, and wind fields over a ~ 100 × 100 m box surrounding the SW2 and WLEF towers. Over all IOPs, 26 (103) flights were conducted with the DJI S-1000 (Meteodrone SSE).

Surface Environment

Data on the ecological environment were collected to provide the boundary conditions of canopy type, activity, and stress, needed for estimating scaling properties. This was done with a variety of methods, including airborne imaging spectroscopy, ground-based phenological characterization, and tree growth measurements.

Foliar functional traits such as leaf mass per area (LMA) and nitrogen concentration strongly influence photosynthetic capacity and plant growth (i.e., net primary production, NPP) (Niinemets 2001; Kattge et al. 2009), and can be mapped using imaging spectroscopy (aka hyperspectral remote sensing, Singh et al. 2015). To map foliar functional traits across the domain a full-range imaging spectroscopy system comprising two co-aligned imagers (VNIR-1800 and SWIR-384; HySpex, Skedsmokorset, Norway) was operated from a Cessna 210 at 1400 m AGL on four days (6/26, 7/11, 8/4, 8/30), producing images with 1 m spatial resolution. The HySpex collects 474 bands with a spectral resolution of 3.26 nm in the VNIR (400-1000 nm) and 5.45 nm in the SWIR (1000-2500 nm).

Extensive ground-based vegetation samples were collected to support the hyperspectral image analyses. These included 41 plots in the domain for measuring tree species (400+ trees), root growth, tree height, diameter at breast height (DBH), net primary production (NPP), biometry, leaf area index (LAI). This also included 122 top-of-canopy foliar samples to estimate leaf level function traits following the protocol from Serbin et al. (2014).

In combination with an existing extensive database of foliar traits and image spectra (Wang et al. in press), we will use the 122 foliar samples to develop and validate 1 m resolution maps for all four dates of numerous foliar functional traits hypothesized to influence NPP, including LMA, nitrogen concentration, chlorophyll and other pigments, phosphorus, non-structural carbohydrates, fiber and lignin, and phenolics). From this, we will test the relationship between functional traits and GPP (as derived from towers) and peak-season integrated NPP (early-July to early-September, derived from the 41 plots). We will generate 1 m maps of NPP and GPP, and identify the foliar factors that most influence each.

Additional plots were used to measure vegetation phenology as it changed through the season, building upon several years of previous phenological observations collected in the domain. Autumn tree leaf color and fall phenology levels were visually observed and recorded at least twice weekly over six weeks during the senescence period (Sep 1 to Oct 25) for a group of 214 individual trees (at ten sites distributed over the 10 ×10 km area) that were representative of the major species.

Forest canopy structure was characterized using an sUAS-based lidar system (Routescene; Edinburgh, Scotland) acquiring high density point clouds (500 pts m^{-2}) within footprints from 11 CHEESEHEAD19 flux tower sites including aspen, pine, poplar, larch, cedar, and hardwood forests. Areas surveyed ranged between 0.25 – 1 km^2 per site. Additional canopy information for the entire domain came from leaf-off LiDAR from USFS sampling (1 m^2 resolution) conducted for the three counties that comprise the study area between 2014 and 2017.

Land surface temperature (LST) is a key environmental driver of the surface energy balance (e.g., Metzger et al., 2013; Xu et al. 2017a). Spatially explicit LST can be acquired from satellite remote sensing (Fig. 5). However, there are tradeoffs in space and time resolutions such that no single sensor provides sufficient resolution for use as a land surface driver to map heat fluxes across space at sub-kilometer and hourly time steps required for the hypotheses here. Also, remote sensing methods may not be able to distinguish between true surface temperature and upper canopy temperature. Here, we are investigating multi-sensor fusion using a combination of in situ thermal drone and infrared camera imagery, ECOSTRESS, Landsat, VIIRS and/or GOES (Wu et al. 2013).

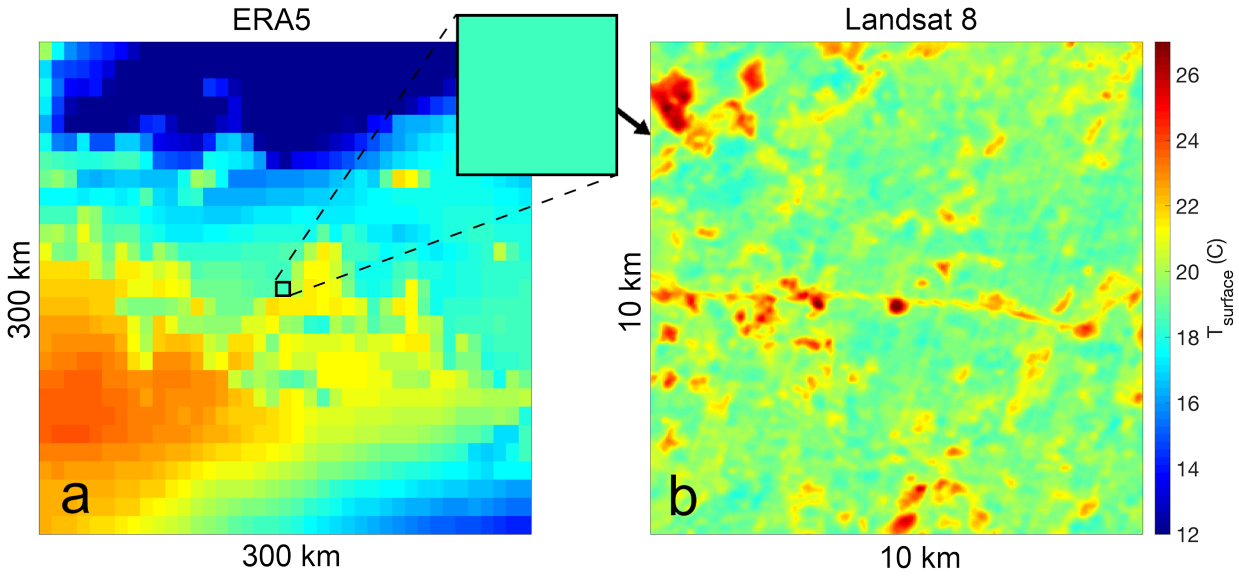

Fig. 5. Land surface temperature on June 15, 2019 from (a) ERA5 reanalysis and (b) derived from Landsat 8, where sub-grid spatial resolution is present, but temporal resolution is low (Gerace et al. 2020; Landsat 8 data courtesy of the U.S. Geological Survey; ERA5 data generated using Copernicus Climate Change Service Information 2020).

Data Analysis & Modeling

Two analytical methods have been proposed to test the hypotheses of this study. The first is the application of ERF-VCV – a data driven approach that can be used to account for the dispersive fluxes missed by single-tower EC measurements, and to upscale fluxes across the CHEESEHEAD19 domain (Metzger, 2018, Xu et al., 2018, Xu et al., 2020). ERF-VCV uses a machine learning algorithm to find relationships between measured fluxes and their meteorological and surface drivers within the flux footprints (see sidebar).

We will perform LES for the IOP days using the Parallelized LES Model PALM (Raasch and Schröter 2001; Maronga et al. 2015; 2020). In the LES we will emulate airborne- and tower-mounted flux observations to compare them against the 'real-world' observations with the ability to also evaluate flux footprints using Lagrangian particle modelling, radiation footprints, storage fluxes at various locations and points in time. To accurately simulate the physical processes as observed during the IOPs of the field experiment as realistically as possible, we will assume realistic topography for the experiment site, and apply a Land Surface Model (LSM) with a coupled soil and radiation model, as well as a Plant Canopy Model (PCM). The use of the LSM and PCM runs instead of prescribed surface fluxes will allow us to study land-atmosphere feedbacks such as self-reinforcement of mesoscale circulations over the heterogeneous study domain. The LSM will be set up for each IOP test case, with land use classes, soil, and

vegetation data as observed during the field experiment. Further, in order to account for synoptic-scale processes during the IOPs (e.g., advection of air masses with different characteristics) we will nest the LES domain into a larger-scale model.

One proposed goal is to derive a parametric heterogeneity correction of dispersive fluxes by setting up virtual towers within the LES, applying it to CHEESEHEAD19 tower flux field data, and evaluating it with ERF-VCV flux grids. Therefore, tower-level turbulence characteristics will be simulated as observed during the field campaign to investigate the energy balance non-closure problem. Additionally, by emulating 'real-world' measurements we intend to help interpret the observations – such as giving hints where secondary circulations occur or how far heterogeneity signals extend downwind.

SIDEBAR: CONTINUITY THROUGH ENVIRONMENTAL RESPONSE FUNCTIONS

CHEESEHEAD19 disentangles how land surface heterogeneity relates to atmospheric transport in mesoscale eddies, which contributes to the discrepancy between EC flux observations and model predictions. We strive to create a new class of observational flux data product that reconciles resulting biases on orders of 10% (Chen et al. 2011; Foken et al. 2011) and reveals actual surface emissions. For non-uniform exchange surfaces such as in CHEESEHEAD19, this requires us to evaluate the conservation of mass and energy continuously in time and space throughout the study domain (e.g., Finnigan 2008). However, even intensive field instrumentation campaigns such as CHEESEHEAD19 cannot produce observations everywhere, all the time. Here, Environmental Response Functions (ERF; Metzger et al. 2013; Metzger 2018) can help attain the necessary information continuum from individual observation plots to model grid scale. To achieve this, ERFs complement information across disciplines and observation types by using a machine learning algorithm to find relationships between measured fluxes and their meteorological and surface drivers within the flux footprints (Fig. 6A). This provides a powerful approach not only for post-field data synthesis, but already in the experiment planning stage e.g. in combination with Large Eddy Simulations (Fig. 6B). Maximizing scientific return on experimental investment (Fig. 6C; Metzger et al., in preparation) is one example of how ERFs can help close the circle among obtaining “knowledge from data” and “data from knowledge” (Reichstein et al. 2019).

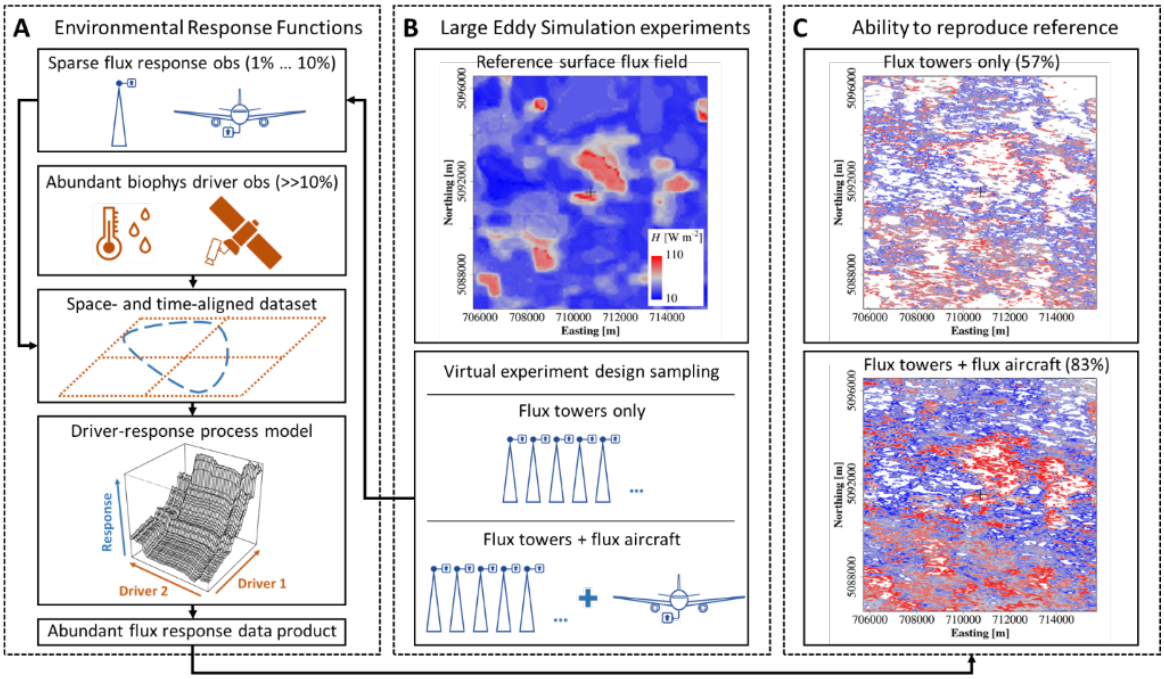

Fig. 6. Panel A: Environmental Response Functions (ERFs) augment sparse response observations (e.g., tower and aircraft EC) with abundant driver observations (e.g., meteorological stations and satellites). High-rate time-frequency decomposition and source area modeling facilitate data joins among these response and driver observations at minute- and meter-scale. Machine learning then extracts a driver-response process model from the resulting space- and time-aligned dataset. Ultimately, this driver-response process model complements the properties of response and driver observations in the response data product. In the present example these are meter-scale sensible heat flux maps, which can be used to more reliably evaluate the conservation of energy across the non-uniform CHEESEHEAD19 experiment domain.

Panel B: During the experiment planning stage we used Large Eddy Simulations (LES) to create synthetic atmospheres over the CHEESEHEAD19 domain for different synoptic conditions. We simultaneously sampled the synthetic atmospheres as observed by different virtual experiment designs. Each experiment design resulted in a separate set of virtual observations which we independently processed through the ERFs in Panel A.

Panel C: We benchmarked the different experiment designs against their ability to reproduce the LES reference in the form of flux grids that ERF reconstructed from the virtual observations alone. Identifying the optimal experiment design not only allowed us to double the scientific return on experimental investment, but also to simplify flight plans and increase crew safety. For additional detail see the full study by Metzger et al. (in preparation).

PRELIMINARY RESULTS

Over the course of the four-month study period the region exhibited light winds (diurnal means from 1 – 4 m s^{-1}) from all directions, with the most prevalent direction being southwesterly (Fig. 7). Air and soil temperatures decreased over the period, while soil moisture increased (Fig. 7b,c). Daily mean net radiation decreased over the course of the study, which showed a direct relationship with ABL height (measured as the height of the inversion on the diurnal radiosonde launches [Fig. 7d]). One of the most relevant seasonal changes with respect to energy balance was the change in the daytime Bowen Ratio (H_S / H_L) which averaged 0.5 in the summer and 1.0 in the fall, with the latter period having more variability than the former. Diurnal cycles of sensible and latent heat flux show that latent heat flux is much larger in the summer when the canopy is fully evapotranspiring compared to the fall, when senescence of broadleaf trees reduces H_L, allowing H_S to comprise a larger share of the total heat flux over the region (Fig. 7f – i).

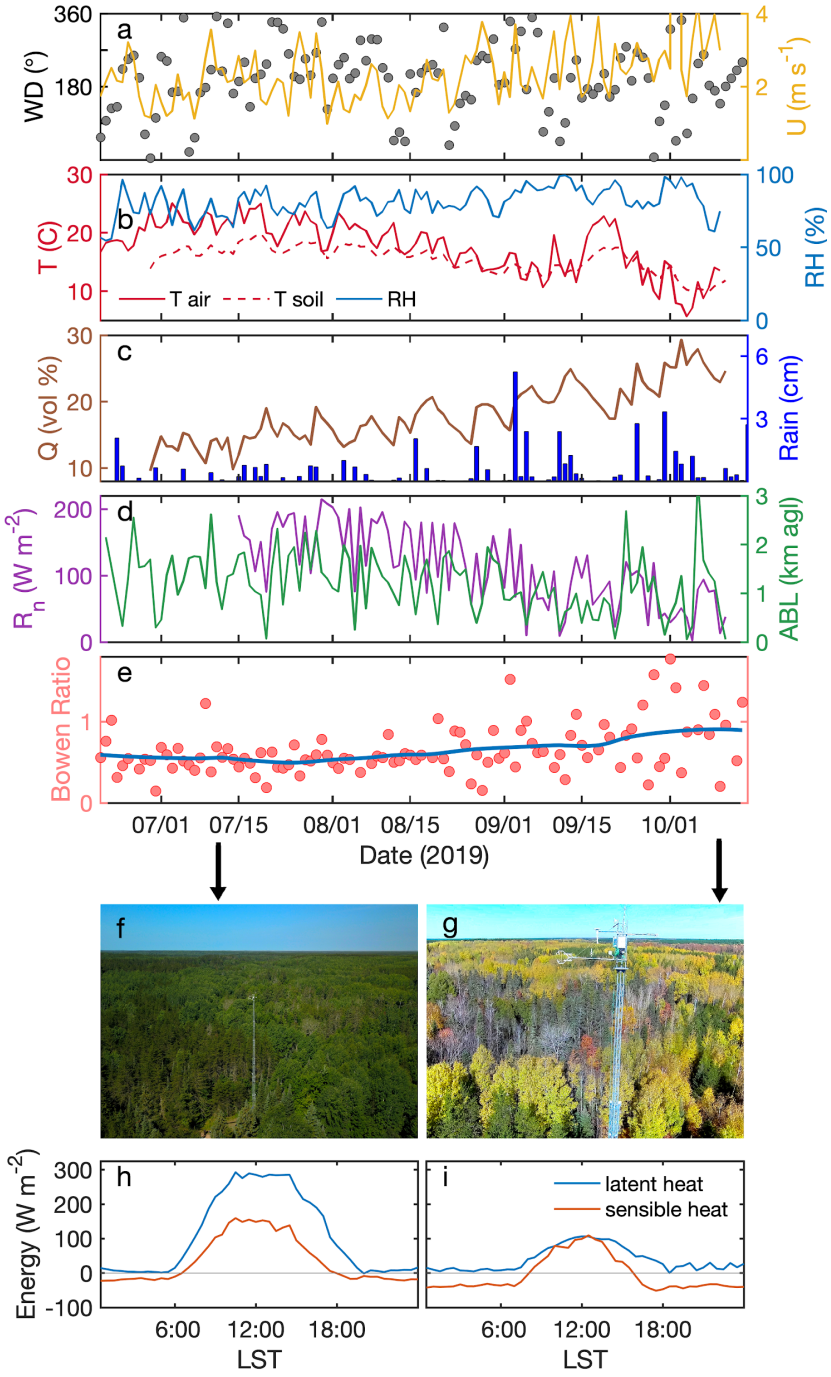

Fig. 7. Daily mean (a) wind speed and direction, (b) temperature and relative humidity, (c) soil moisture, (d) net radiation and ABL height, and (e) Bowen ratio averaged across all ISFS towers. Aerial view of site NE2 on (f) July 12, 2020 and (g) October 9, 2020. Diurnal cycles of sensible and latent heat averaged across all ISFS sites for the weeks of (h) Oct. 4 – 11 and (i) July 7 – 14.

Continuous data collection throughout the campaign linked the energy balance components to the remotely sensed atmospheric environment (Fig. 8). As is typical for EC measurements, we observed energy fluxes that were lower in magnitude than the net incoming energy ($R_N - G$), when averaged across all sites. The magnitudes of the energy balance residual (C_{EB}) was largest during the daytime, when incoming solar radiation was highest. The opposite sign of C_{EB} from day to night in part can be attributed to heat storage in the canopy. However, the magnitudes of the daytime values are larger than the nighttime values, which results in a daily mean imbalance.

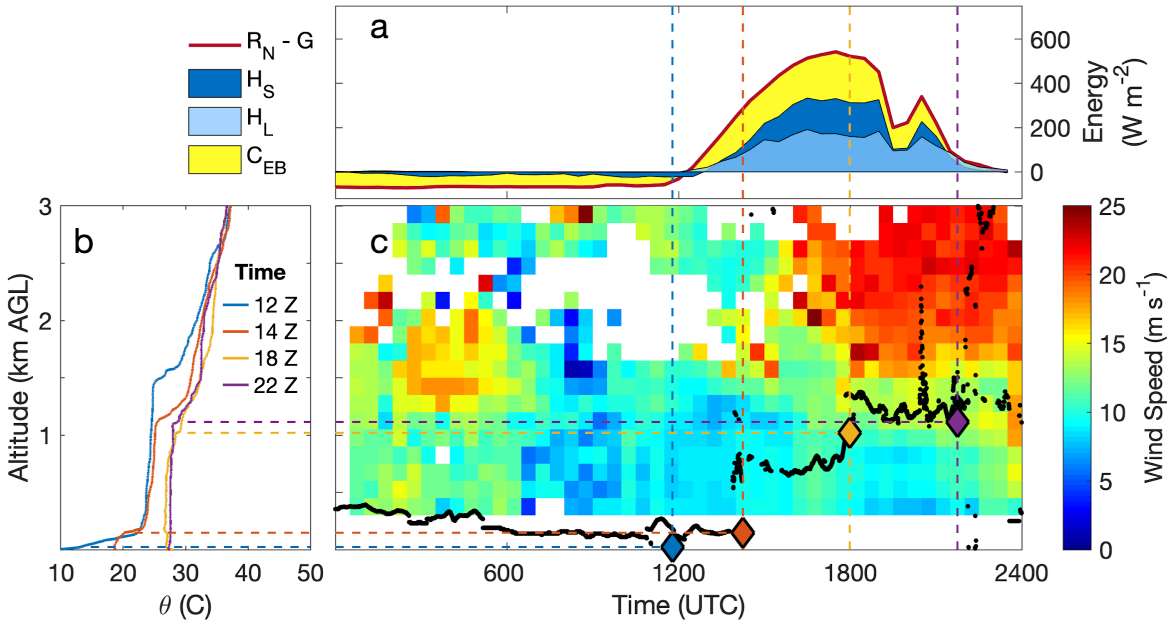

Fig. 8. (a) Stacked energy balance components: net radiation minus ground heat flux (R_N - G), sensible and latent heat flux (H_S and H_L), and energy balance residual (C_{EB}) on Sep 24, 2019; (b) radiosonde profiles of potential temperature (ϑ); and (c) time series of wind speed profile with overlaid ABL height from ceilometer (black dots) and radiosondes (colored diamonds and dashed lines correspond to radiosonde launches in (b)).

The energy balance residual peaked under conditions of low turbulence (Fig. 9). It is during such periods of calm wind and strongly unstable stratification in which thermally-induced mesoscale eddies resulting from landscape-scale heterogeneity are expected (Steinfeld et al. 2007). This lends support to the hypothesis that mesoscale eddies are responsible for the energy balance non-closure.

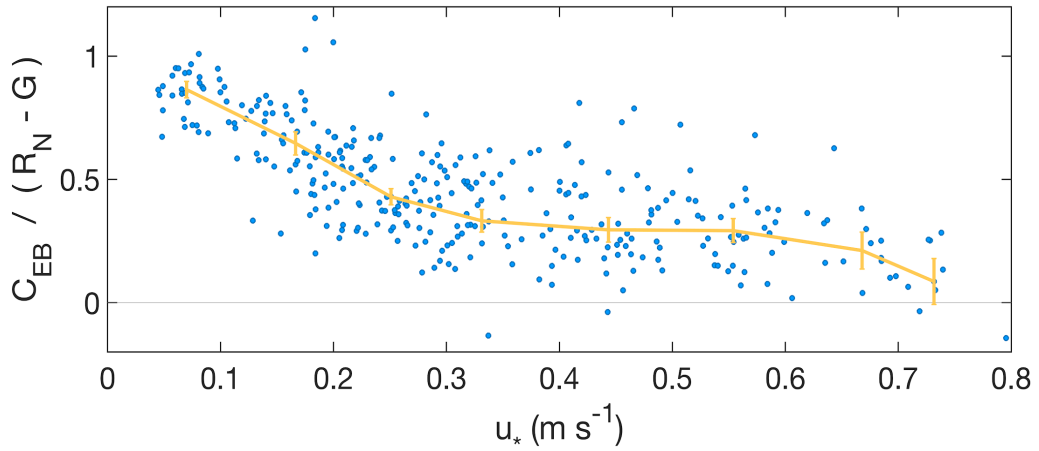

Fig. 9. Daily mean energy balance residuals (C_{EB}) normalized by net radiation minus ground heat flux (R_N - G) plotted against friction velocity (u_*) for all ISFS EC towers for the entire CHEESEHEAD19 dataset (excludes individual towers on days without complete quality-controlled data).

Tower measurements, combined with in-situ measurements of air temperature and land surface temperature from the DJI S-1000, were used to quantify variability in surface H_S following Lee et al. [2017], as shown in an example from 12 Jul 2019 (Fig. 10). On this day, as well as others, there was significant temperature and H_S variability; temperature (H_S) differences were ~ 10°C (100 W m^{-2}) over the ~ 500 × 500 m area surrounding the SW2 tower. Fig. 10 illustrates even finer scale resolution of surface temperature than the measures shown in Fig. 5. Such spatial variation is directly related to underlying surface characteristics.

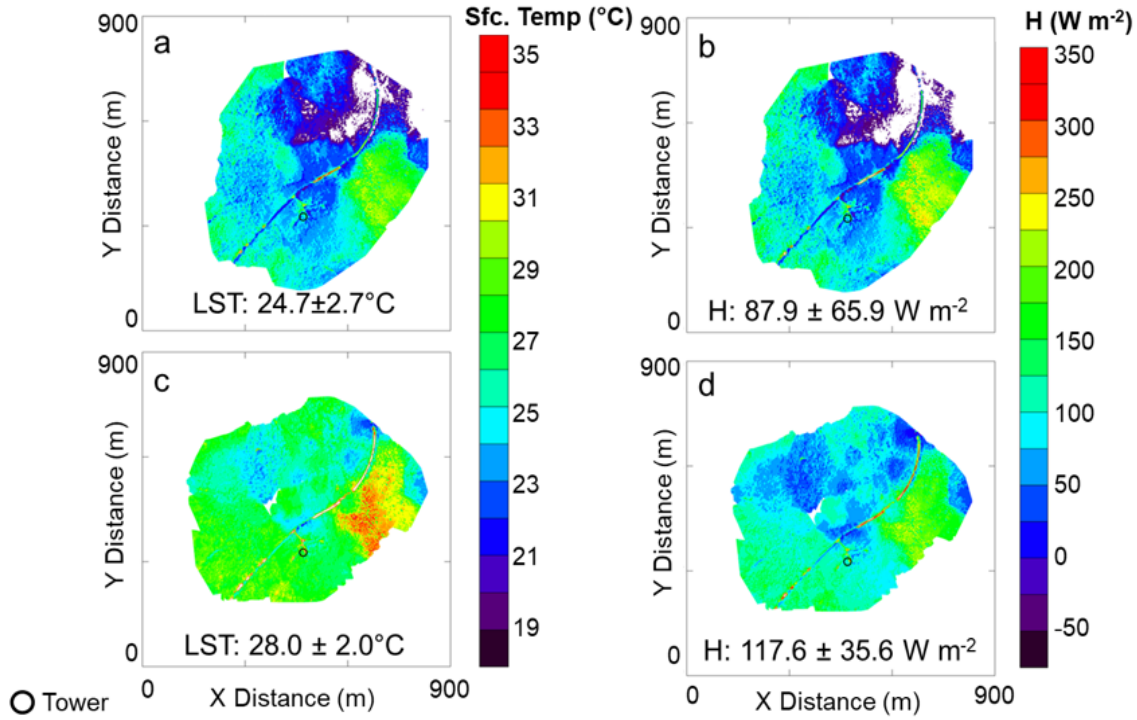

Fig. 10. Surface temperature (a) and H_s (b) from a downward-pointing infrared camera flown on the DJI S-1000 sUAS surrounding the SW2 tower between 1504 and 1518 UTC 12 Jul 2019. Same for panels (c) and (d), but between 1614 and 1628 UTC 12 Jul 2019. H_s computed following Lee et al. (2017). As the technique requires an initial H_s to derive the variability in H_s and H_s was unavailable from SW2 on 12 Jul, H_s at SW2 was estimated using a linear regression with data from nearby towers. Mean ± 1 standard deviation shown at the bottom of each panel.

Landscape heterogeneity was observed for a range of environmental variables, including vegetation spectral characteristics and canopy height captured from downward-looking airborne remote sensing instruments (Fig. 11). False color HySpex imagery is being used to differentiate plant functional types at 1 m^2 resolution. Additional information on leaf-on canopy structure, obtained from the Routescene LiDAR at 11 flux sites and across the entire domain from the State of Wisconsin leaf-off LiDAR dataset, are being used to identify surface roughness in the flux footprints of the EC towers. In addition, these spatial data are being used as input drivers within the ERF-VCV machine learning approach.

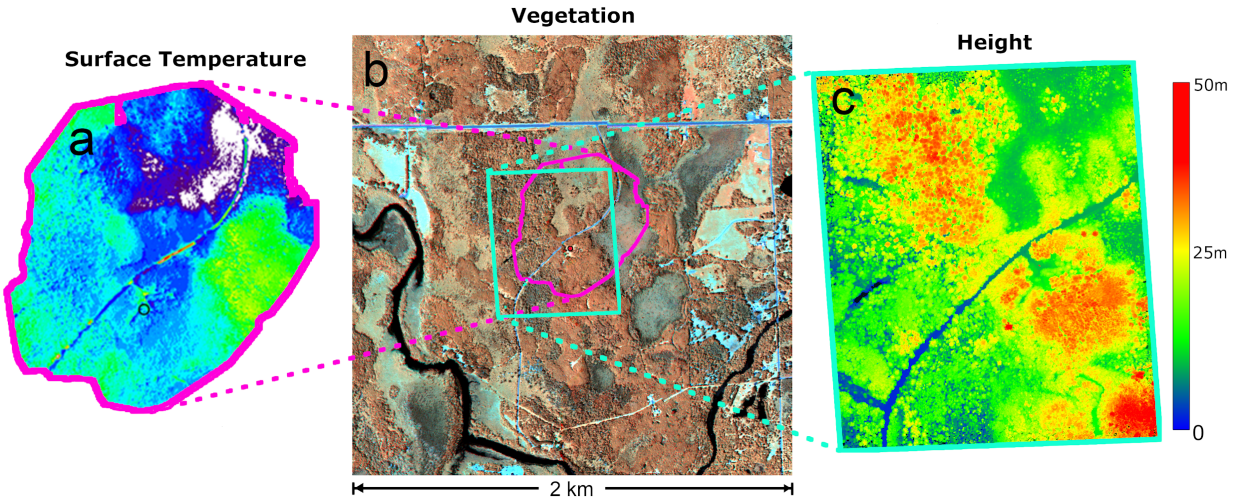

Fig. 11. Surface maps showing spatial variation around tower site SW2 in (a) surface temperature measured by the DJI S-1000 (same as Fig. 10a), (b) vegetation spectral characteristics measured by the HySpex shown as a false color image (849 nm – red, 1650 nm – green, 2217 nm – blue), and (c) surface/canopy height measured by the sUAS Routescene lidar.

There is also spatial variation in the energy balance components across the domain on a typical day (Fig. 12a). This variability includes the relative weighting of latent and sensible heat fluxes, as well as the magnitude of the energy balance residual. The mean energy balance closure (calculated as $[H_S + H_L]/[R_N - G]$) across all the sites over the entire study period was 0.8 This is typical for EC towers and supports the need for the advanced methods put forth by this study.

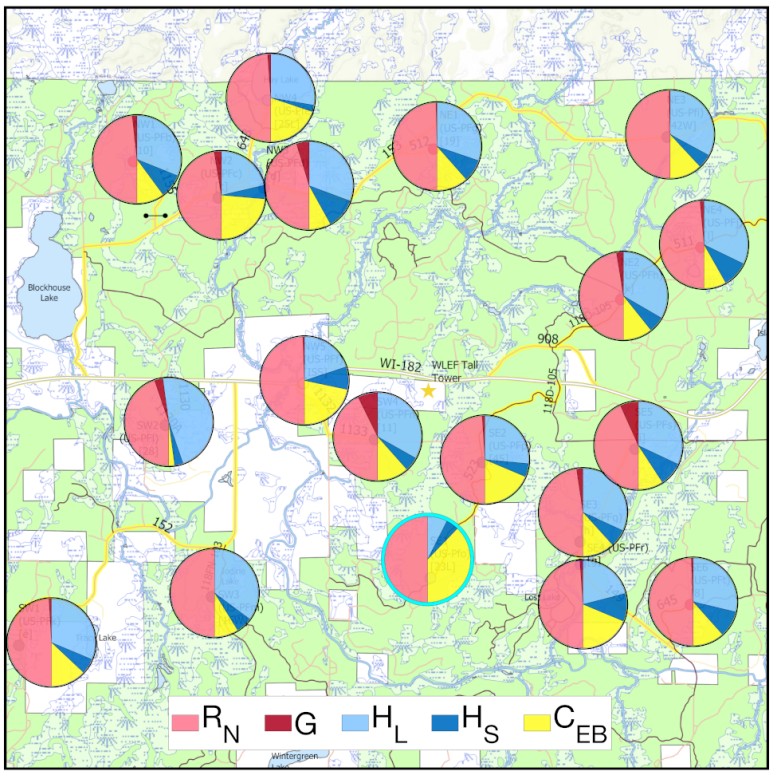

Fig. 12. Average daily mean energy balance pie charts for the flux towers over the entire study period. The pie chart with the cyan outline (bottom center) was a buoy EC system deployed on a small lake.

To address this spatial and temporal variability we are testing different types of spatial EC techniques, which have been suggested as a means of mitigating errors arising from single-site EC (Steinfeld et al. 2007; Mauder et al. 2008b). Using LES, Xu et al. (2020) found that standard spatial EC improved closure over standard temporal EC, while a combined spatio-temporal method performed better still. Further, by applying the ERF-VCV approach, the energy balance was found to be almost completely closed.

Here we had the ability to calculate spatial fluxes from two different sources. First, the spatial fluxes were calculated using a wavelet decomposition on the aircraft EC datasets. This dataset has good spatial coverage but limited temporal resolution, though, with 72 flight hours spread across 12 days, it is one of the largest airborne EC datasets ever collected.

The second data source for spatial EC was the set of 20 flux towers spread across the domain. Calculations for flux footprints on Sep 26, 2019 (Fig. 13) show that spatial coverage of the towers (including WLEF) covered roughly 8% of the domain (using Kljun et al. [2015]). This is a significant increase compared to a single tower set up (typically <<1% of a 10 × 10 km area). An additional benefit from the experiment design is that the towers cover a range of physical environments. These data are being used to confirm the LES model results for improvements to

energy balance closure. By combining the tower and aircraft EC datasets we have excellent coverage (~80%) of the study domain on flight days (Fig. 13).

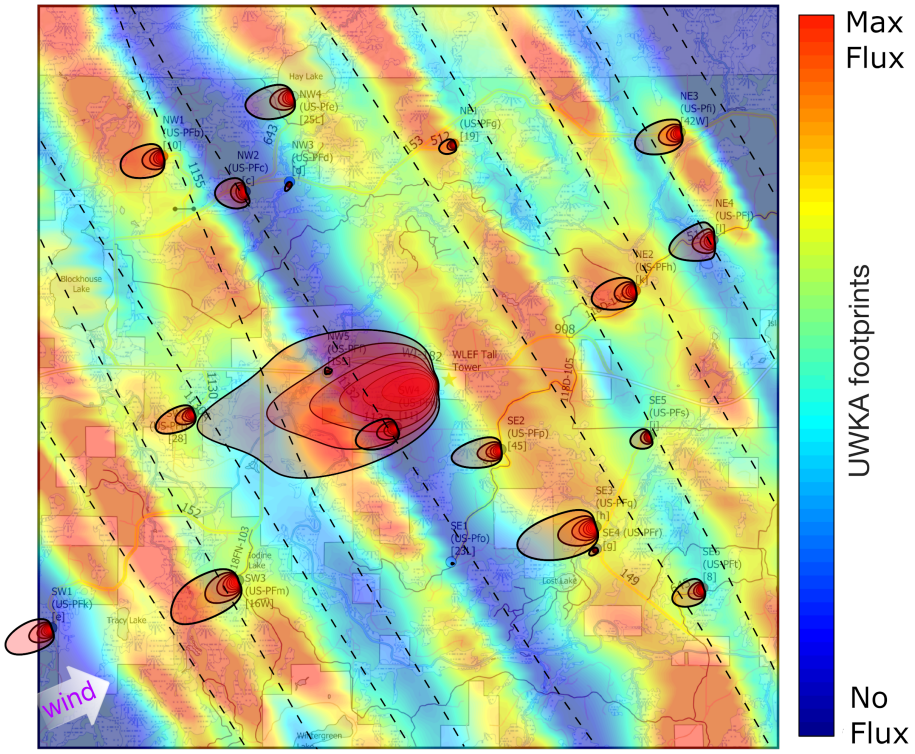

Fig. 13. Flux footprint climatologies from the 20 flux towers and aircraft on the morning of September 26, 2019. Tower footprints extend to the 90% footprint with 10% contour lines shown down to 10% (calculated based on Kljun et al. [2015]). The heat map shows aircraft flux footprints with areas of strongest flux contribution in red, grading to blue where there was no contribution (calculated based on Metzger et al. [2013]). UWKA flight tracks shown as dashed black lines.

The characterization of the ABL and identification of mesoscale eddies will be performed using lidar measurements of wind, water vapor, temperature, and backscatter. Figure 14 shows an example of this on September 24. Increasing water vapor through the day is representative of a large-scale warm, wet airmass entering the domain (Fig. 14c,d; Fig. S2a). This characterizes the variation in water vapor throughout the collection of the morning UWKA CRL dataset (Fig. 14a). The afternoon CRL dataset (Fig. 14b) shows a more evenly mixed ABL, with variation in water vapor due to local pockets of relatively moist and dry air. These two examples show the varying applications of the CRL data depending on the atmospheric environment, with the afternoon flight illustrating the potential of the dataset for determining the degree of ABL heterogeneity arising from surface heterogeneity. Further analysis will investigate relationships with underlying vegetation and LST.

Around 1200 UTC (7am local time) net radiation becomes positive (Fig. 8a) and soon after we see the breakup of the surface inversion (Fig. 14d). Around 1400 – 1500 UTC we see the ABL grow (Fig. 8c) followed by development of large-scale structures revealed by strong oscillations in vertical wind speed (±2 m s^{-1}; Fig. 14e). During peak hours the angle of attack of the wind vectors oscillate between roughly -30º to 50º degrees on time scales of 10 minutes to an hour. These angles far exceed those of the underlying terrain, suggesting that these periodic updrafts and downdrafts are the result of mesoscale eddies.

Around 1900 UTC the domain clouds over, seen in R_N and backscatter (Fig. 8a; Fig. 14f; Fig. S2b). This causes the strength of the oscillation in vertical wind to decrease (Fig. 14e), which coincides with a change in the relative weighting of the different energy balance components, with both R_N and H_S decreasing strongly, while H_L decreases only slightly (Fig. 8a). An increase in R_N around 2000 UTC corresponds to strengthening vertical wind speed oscillations. Further analyses will investigate the prevalence of this result across the entire dataset and examine specific drivers and possible implications for EC energy balance closure. These datasets show that changes in ABL development are closely tied to changes in the surface energy fluxes, highlighting the potential research applications of the CHEESEHEAD19 data.

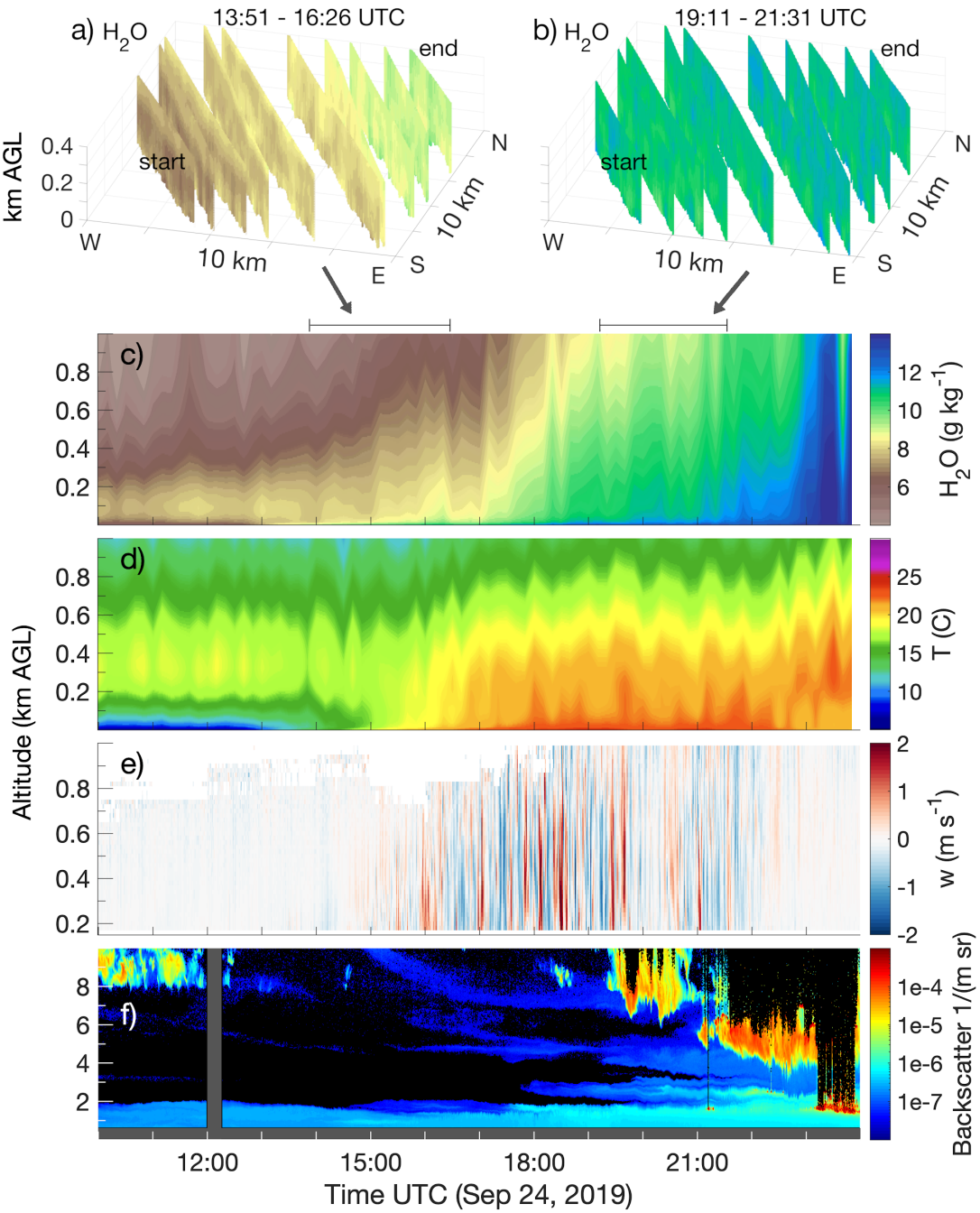

Fig. 14. (a) and (b) show CRL cross sections of H_2O mixing ratio (cut to domain size; panel c colorbar represents panels a - c) for each of 10 legs on Research Flights 17 and 18 (Sep 24 at 13:51 - 16:26 and 19:11 - 21:31 UTC); time series profiles of (c) H_2O mixing ratio and (d) T measured by the ground-based MWR, (e) vertical wind speed calculated using the ground-based RHI scanning wind lidars (L_A, L_B) for the column above L_{VS}, and (f) 532 nm backscatter from the ground-based HSRL at WLEF tall tower on Sep 24, 2019.

EDUCATIONAL OUTREACH

Several public events were conducted to introduce and communicate the science goals and objectives of the project. These include a pre-experiment community-wide public presentation at the Park Falls Public Library and a summer open house at several sites, enabling members of the community to visit data collection locations, meet CHEESEHEAD19 team members, and participate in demonstrations of the instruments. CHEESEHEAD19 team members also participated in surveys and in training on fieldwork bullying and sexual harassment prevention (Fischer et al. in review).

The project also worked with two local school groups, one from Butternut, Wisconsin K-12 School and another from Chequamegon High School of Park Falls, WI, to include them as supporting data collectors. The GLOBE (Global Learning and Observations to Benefit the Environment) program trained Butternut K-12 students and a teacher to collect land cover classification data, soil properties, and atmospheric data at seven of the tower sites at multiple times throughout the summer. The high school group installed ten tree temperature sensors at five of the forest flux tower sites, which are being used to estimate biomass heat storage. We also hosted two undergraduate university field classes (UW-Madison and U-South Carolina), which conducted independent research projects on micrometeorology and carbon cycling.

Fig. 15. Bill Brown (just right of the radiosonde balloon) describing the capabilities of the ISS facility during the community open house.

DATA AND CODE AVAILABILITY

The database of observations and models is currently online and freely available to the community and public for general use or for further scientific investigation. The datasets and supporting information have been gathered together in the NCAR Earth Observatory Laboratory (EOL) data repository which can be accessed through the project web page at https://www.eol.ucar.edu/field_projects/cheesehead. The project has open data and code policies, in which other researchers are encouraged to use CHEESEHEAD19 resources for their own research. The policies can be accessed through the above web page.

Additionally, data are stored and are being used for in-depth analysis and modeling purposes on the NSF-funded cloud computing platform CyVerse, with the goal of having a central location for users to bring their code to the data in a way that maintains data and code provenance for collaborative, multi-user projects. Additional information about the project, including descriptions of the sites, photographs, and data plots can be found on the CHEESEHEAD19 website, located at www.cheesehead19.org.

CONCLUSIONS

The data collected during the CHEESEHEAD19 field campaign show a distinct seasonal shift in surface energy fluxes, as well as spatial patterning that appears to be directly related to the characteristics of the underlying surface environment. Consequently, the imbalance in the energy budget displays both temporal and spatial variability, with the imbalance becoming larger under periods of low turbulence. The broad coverage of the measured fluxes using the 20-tower network and airborne EC, combined with the collection of spatial data of surface characteristics like LST, vegetation type, and canopy structure, will enable thorough investigation of the causes of energy balance non-closure. Additionally, the suite of atmospheric profiling instrumentation characterizes the mesoscale structure of atmospheric flows over the study domain to an unprecedented degree, helping to determine how mesoscale eddies contribute to measured imbalances. The observational dataset provided by CHEESEHEAD19 will also enable the use of machine-learning approaches and LES for testing hypotheses on scaling and parameterization of sub-grid processes in mesoscale meteorological models. Findings emerging from this project are expected to have broad implications for heterogeneous terrestrial regions beyond the specific study domain.

APPENDIX: LIST OF ACRONYMS

AGL – above ground level
ARL - Air Resources Laboratory (NOAA)
ATDD – Atmospheric Turbulence and Diffusion Division (NOAA)
CHEESEHEAD19 – Chequamegon Heterogeneous Ecosystem Energy-balance Study Enabled by a High-density Extensive Array of Detectors 2019
CLAMPS – Collaborative Lower Atmospheric Mobile Profiling System (NOAA NSSL)
CRL – Compact Raman Lidar

EC – Eddy Covariance
GML – Global Monitoring Laboratory (NOAA)
IOP – Intensive Observation Period
LES – Large Eddy Simulation
lidar – light detection and ranging
LSM – Land Surface Model
NCAR – National Center for Atmospheric Research
NOAA – National Atmospheric and Oceanic Administration
NSF – National Science Foundation
NSSL – National Severe Storms Laboratory (NOAA)
PALM – Parallelized LES Model
PSL – Physical Sciences Laboratory (NOAA)
radar – radio detection and ranging
RASS – Radio Acoustic Sounding System
sodar – sonic detection and ranging
sUAS - small Unmanned Aircraft System
SURFRAD – Surface Radiation Budget Network
UWKA – University of Wyoming King Air

APPENDIX: LIST OF VARIABLES

F_{CO2} – CO_2 flux (μmol m^{-2} s^{-1})
G – Ground heat flux (W m^{-2})
H_2O – water vapor mixing ratio (g kg^{-1})
H_S – sensible heat flux (W m^{-2})
H_L – latent heat flux (W m^{-2})
LST – land surface temperature (C)
P – Pressure (mbar)
R_N – Net surface radiation (W m^{-2})
T – temperature (C)
T_v – virtual temperature (C)
U – horizontal wind speed (m s^{-1})
u_* – friction velocity (m s^{-1})
w – vertical wind speed (m s^{-1})
θ – potential temperature (C)
θ_v – virtual potential temperature (C)
τ – momentum flux (N m^{-2})

ACKNOWLEDGEMENTS

We would like to acknowledge operational, technical, and scientific support provided by NCAR's Earth Observing Laboratory, sponsored by the National Science Foundation. We also acknowledge the technical and scientific contributions from teams at NOAA, National Ecological Observatory Network (NEON), KIT, University of Wyoming, and University of Wisconsin. We are grateful for the support provided by the US Forest Service and Wisconsin

Educational Communication Board. CHEESEHEAD19 would not have been possible without the contributions from many additional groups and individuals, who are listed in the supplemental materials. This project was financially supported by NSF Award #1822420, Deutsche Forschungsgemeinschaft (DFG) Award #406980118, Wisconsin Alumni Research Foundation WARF UW Fall Competition Award, the Department of Energy American Network Management Project support of the ChEAS core site cluster, and NSF Award #1918850. The cross-lab NOAA contribution was supported by the Weather Program Office in the Office of Oceanic and Atmospheric Research. We acknowledge that this project occurred on the traditional territory of the Ojibwe people.

REFERENCES

Anderson, M., J. Norman, W. Kustas, R. Houborg, P. Starks, and N. Agam, 2008: A thermal-based remote sensing technique for routine mapping of land-surface carbon, water and energy fluxes from field to regional scales. *Remote Sens. Environ.*, **112**, 4227–4241, https://doi.org/10.1016/j.rse.2008.07.009.

Anderson, M. C., and Coauthors, 2012: Mapping daily evapotranspiration at Landsat spatial scales during the BEAREX'08 field campaign. *Adv. Water Resour.*, **50**, 162–177, https://doi.org/10.1016/j.advwatres.2012.06.005.

Antonarakis, A. S., J. W. Munger, and P. R. Moorcroft, 2014: Imaging spectroscopy- and lidar-derived estimates of canopy composition and structure to improve predictions of forest carbon fluxes and ecosystem dynamics. *Geophys. Res. Lett.*, **41**, 2535–2542, https://doi.org/10.1002/2013GL058373.

Aubinet, M., and Coauthors, 2010: Direct advection measurements do not help to solve the night-time CO2 closure problem: Evidence from three different forests. *Agric. For. Meteor.*, **150**, 655–664, https://doi.org/10.1016/j.agrformet.2010.01.016.

Avissar, R., 1995: Scaling of land-atmosphere interactions: An atmospheric modelling perspective. *Hydrol. Process.*, **9**, 679–695, https://doi.org/doi:10.1002/hyp.3360090514.

Bakwin, P. S., P. P. Tans, D. F. Hurst, and C. Zhao, 1998: Measurements of carbon dioxide on very tall towers: results of the NOAA/CMDL program. *Tellus B Chem. Phys. Meteor.*, **50**, 401–415, https://doi.org/10.3402/tellusb.v50i5.16216.

Barnard, J. C., and C. N. Long, 2004: A Simple Empirical Equation to Calculate Cloud Optical Thickness Using Shortwave Broadband Measurements. *J. Appl. Meteor.*, **43**, 1057–1066, https://doi.org/10.1175/1520-0450(2004)043<1057:ASEETC>2.0.CO;2.

Barr, J. G., J. D. Fuentes, M. S. DeLonge, T. L. O'Halloran, D. Barr, and J. C. Zieman, 2013: Summertime influences of tidal energy advection on the surface energy balance in a mangrove forest. *Biogeosciences*, **10**, 501–511, https://doi.org/10.5194/bg-10-501-2013.

Bertram, T. H., and Coauthors, 2011: A field-deployable, chemical ionization time-of-flight mass spectrometer. *Atmos. Meas. Tech.*, **4**, 1471–1479, https://doi.org/10.5194/amt-4-1471-2011.

Betts, A. K., J. H. Ball, A. C. M. Beljaars, M. J. Miller, and P. A. Viterbo, 1996: The land surface-atmosphere interaction: A review based on observational and global modeling perspectives. *J. Geophys. Res. Atmos.*, **101**, 7209–7225, https://doi.org/10.1029/95JD02135.

Beyrich, F., and Coauthors, 2006: Area-Averaged Surface Fluxes Over the Litfass Region Based on Eddy-Covariance Measurements. *Bound.-Layer Meteor.*, **121**, 33–65, https://doi.org/10.1007/s10546-006-9052-x.

Blumberg, W. G., D. D. Turner, U. Löhnert, and S. Castleberry, 2015: Ground-Based Temperature and Humidity Profiling Using Spectral Infrared and Microwave Observations.

914 Part II: Actual Retrieval Performance in Clear-Sky and Cloudy Conditions. *J. Appl. Meteor.*
915 *Climatol.*, **54**, 2305–2319, https://doi.org/10.1175/JAMC-D-15-0005.1.

916 Calhoun, R., R. Heap, M. Princevac, R. Newsom, H. Fernando, and D. Ligon, 2006: Virtual
917 Towers Using Coherent Doppler Lidar during the Joint Urban 2003 Dispersion Experiment.
918 *J. Appl. Meteor. Climatol.*, **45**, 1116–1126, https://doi.org/10.1175/JAM2391.1.

919 Cammalleri, C., M. C. Anderson, G. Ciraolo, G. D'Urso, W. P. Kustas, G. La Loggia, and M.
920 Minacapilli, 2012: Applications of a remote sensing-based two-source energy balance
921 algorithm for mapping surface fluxes without in situ air temperature observations. *Remote*
922 *Sens. Environ.*, **124**, 502–515, https://doi.org/10.1016/j.rse.2012.06.009.

923 Charney, J. G., 1975: Dynamics of deserts and drought in the Sahel. *Q. J. R. Meteor. Soc.*, **101**,
924 193–202, https://doi.org/doi:10.1002/qj.49710142802.

925 Charuchittipan, D., W. Babel, M. Mauder, J.-P. Leps, and T. Foken, 2014: Extension of the
926 Averaging Time in Eddy-Covariance Measurements and Its Effect on the Energy Balance
927 Closure. *Bound.-Layer Meteor.*, **152**, 303–327, https://doi.org/10.1007/s10546-014-9922-6.

928 Chen, B., and Coauthors, 2011: Assessing eddy-covariance flux tower location bias across the
929 Fluxnet-Canada Research Network based on remote sensing and footprint modelling. *Agric.*
930 *For. Meteor.*, **151**, 87–100, https://doi.org/10.1016/j.agrformet.2010.09.005.

931 Cook, B. D., and Coauthors, 2004: Carbon exchange and venting anomalies in an upland
932 deciduous forest in northern Wisconsin, USA. *Agric. For. Meteor.*, **126**, 271–295,
933 https://doi.org/10.1016/j.agrformet.2004.06.008.

934 Davis, K. J., P. S. Bakwin, C. Yi, B. W. Berger, C. Zhao, R. M. Teclaw, and J. G. Isebrands,
935 2003: The annual cycles of CO2 and H2O exchange over a northern mixed forest as
936 observed from a very tall tower. *Glob. Chang. Biol.*, **9**, 1278–1293,
937 https://doi.org/10.1046/j.1365-2486.2003.00672.x.

938 Desai, A. R., P. V. Bolstad, B. D. Cook, K. J. Davis, and E. V. Carey, 2005: Comparing net
939 ecosystem exchange of carbon dioxide between an old-growth and mature forest in the
940 upper Midwest, USA. *Agric. For. Meteor.*, **128**, 33–55,
941 https://doi.org/10.1016/j.agrformet.2004.09.005.

942 ——, K. J. Davis, C. J. Senff, S. Ismail, E. V. Browell, D. R. Stauffer, and B. P. Reen, 2006: A
943 Case Study on the Effects of Heterogeneous Soil Moisture on Mesoscale Boundary-Layer
944 Structure in the Southern Great Plains, U.S.A. Part I: Simple Prognostic Model. *Bound.-*
945 *Layer Meteor.*, **119**, 195–238, https://doi.org/10.1007/s10546-005-9024-6.

946 Desai, A. R., B. R. Helliker, P. R. Moorcroft, A. E. Andrews, and J. A. Berry, 2010: Climatic
947 controls of interannual variability in regional carbon fluxes from top-down and bottom-up
948 perspectives. *J. Geophys. Res. Biogeosciences*, **115**,
949 https://doi.org/doi:10.1029/2009JG001122.

950 Dürr, B., and R. Philipona, 2004: Automatic cloud amount detection by surface longwave
951 downward radiation measurements. *J. Geophys. Res.*, **109**, D05201,
952 https://doi.org/10.1029/2003JD004182.

953 Eder, F., M. Schmidt, T. Damian, K. Träumner, and M. Mauder, 2015: Mesoscale eddies affect
954 near-surface turbulent exchange: Evidence from lidar and tower measurements. *J. Appl.*
955 *Meteor. Climatol.*, **54**, 189–206, https://doi.org/10.1175/JAMC-D-14-0140.1.

956 Eloranta, E. W., 2005: High spectral resolution lidar. *Lidar: Range-Resolved Optical Remote*
957 *Sensing of the Atmosphere*, K. Weitkamp, Ed., Springer-Verlag, 143–163.

958 Engelmann, C., and C. Bernhofer, 2016: Exploring Eddy-Covariance Measurements Using a
959 Spatial Approach: The Eddy Matrix. *Bound.-Layer Meteor.*, **161**, 1–17,
960 https://doi.org/10.1007/s10546-016-0161-x.

961 Finnigan, J., 2008: An introduction to flux measurements in difficult conditions. *Ecol. Appl.*, **18**,
962 1340–1350, https://doi.org/10.1890/07-2105.1.

963 Emily V. Fischer, Brittany Bloodhart, Kristen Rasmussen, Ilana B. Pollack, Meredith G.
964 Hastings, Erika Marin-Spiotta, Ankur R. Desai, Joshua P. Schwarz, Stephen Nesbitt, and
965 Deanna Hence, 2020. Leveraging Field-Campaign Networks to Effect Collaborative
966 Change on Sexual Harassment, Bulletin of the AMS, submitted.

967 Foken, T., M. Aubinet, J. J. Finnigan, M. Y. Leclerc, M. Mauder, and K. T. Paw U, 2011:
968 Results Of A Panel Discussion About The Energy Balance Closure Correction For Trace
969 Gases. *Bull. Amer. Meteor. Soc.*, **92**, ES13–ES18,
970 https://doi.org/10.1175/2011BAMS3130.1.

971 Frank, J. M., W. J. Massman, and B. E. Ewers, 2013: Underestimates of sensible heat flux due to
972 vertical velocity measurement errors in non-orthogonal sonic anemometers. *Agric. For.*
973 *Meteor.*, **171**–**172**, 72–81, https://doi.org/https://doi.org/10.1016/j.agrformet.2012.11.005.

974 Gantner, L., V. Maurer, N. Kalthoff, and O. Kiseleva, 2017: The Impact of Land-Surface
975 Parameter Properties and Resolution on the Simulated Cloud-Topped Atmospheric
976 Boundary Layer. *Bound.-Layer Meteor.*, **165**, 475–496, https://doi.org/10.1007/s10546-017-
977 0286-6.

978 Gao, Z., H. Liu, E. S. Russell, J. Huang, T. Foken, and S. P. Oncley, 2016: Large eddies
979 modulating flux convergence and divergence in a disturbed unstable atmospheric surface
980 layer. *J. Geophys. Res. Atmos.*, **121**, 1475–1492, https://doi.org/10.1002/2015JD024529.

981 Garratt, J. R., 1993: Sensitivity of Climate Simulations to Land-Surface and Atmospheric
982 Boundary-Layer Treatments-A Review. *J. Clim.*, **6**, 419–448, https://doi.org/10.1175/1520-
983 0442(1993)006<0419:SOCSTL>2.0.CO;2.

984 Gerace, A., T. Kleynhans, R. Eon, and M. Montanaro, 2020: Towards an Operational, Split
985 Window-Derived Surface Temperature Product for the Thermal Infrared Sensors Onboard
986 Landsat 8 and 9. *Remote Sens.*, **12**, 224, https://doi.org/10.3390/rs12020224.

987 van Heerwaarden, C. C., J. P. Mellado, and A. De Lozar, 2014: Scaling Laws for the
988 Heterogeneously Heated Free Convective Boundary Layer. *J. Atmos. Sci.*, **71**, 3975–4000,
989 https://doi.org/10.1175/jas-d-13-0383.1.

990 Hilker, T., F. G. Hall, N. C. Coops, J. G. Collatz, T. A. Black, C. J. Tucker, P. J. Sellers, and N.

Grant, 2013: Remote sensing of transpiration and heat fluxes using multi-angle observations. *Remote Sens. Environ.*, **137**, 31–42, https://doi.org/10.1016/j.rse.2013.05.023.

Hill, T. C., M. Williams, and J. B. Moncrieff, 2008: Modeling feedbacks between a boreal forest and the planetary boundary layer. *J. Geophys. Res. Atmos.*, **113**, https://doi.org/doi:10.1029/2007JD009412.

——, ——, F. I. Woodward, and J. B. Moncrieff, 2011: Constraining ecosystem processes from tower fluxes and atmospheric profiles. *Ecol. Appl.*, **21**, 1474–1489, https://doi.org/doi:10.1890/09-0840.1.

Kampe, T. U., J. McCorkel, L. Hamlin, R. O. Green, K. S. Krause, and B. R. Johnson, 2011: Progress in the development of airborne remote sensing instrumentation for the National Ecological Observatory Network. W. Gao, T.J. Jackson, J. Wang, and N.-B. Chang, Eds., 81560A.

Kang, S.-L., K. J. Davis, and M. LeMone, 2007: Observations of the ABL Structures over a Heterogeneous Land Surface during IHOP_2002. *J. Hydrometeor.*, **8**, 221–244, https://doi.org/10.1175/JHM567.1.

Kattge, J., W. Knorr, T. Raddatz, and C. Wirth, 2009: Quantifying photosynthetic capacity and its relationship to leaf nitrogen content for global-scale terrestrial biosphere models. *Glob. Chang. Biol.*, **15**, 976–991, https://doi.org/10.1111/j.1365-2486.2008.01744.x.

Klein, P., and Coauthors, 2015: LABLE: A Multi-Institutional, Student-Led, Atmospheric Boundary Layer Experiment. *Bull. Amer. Meteor. Soc.*, **96**, 1743–1764, https://doi.org/10.1175/BAMS-D-13-00267.1.

Kljun, N., P. Calanca, M. W. Rotach, and H. P. Schmid, 2015: A simple two-dimensional parameterisation for Flux Footprint Prediction (FFP). *Geosci. Model Dev.*, **8**, 3695–3713, https://doi.org/10.5194/gmd-8-3695-2015.

Klugmann, D., K. Heinsohn, and H. J. Kirtzel, 1996: A low cost 24 GHz FM-CW Doppler radar rain profiler. *Contrib. Atmos. Phys.*, **61**, 247–253.

Kneifel, S., M. Maahn, G. Peters, and C. Simmer, 2011: Observation of snowfall with a low-power FM-CW K-band radar (Micro Rain Radar). *Meteor. Atmos. Phys.*, **113**, 75–87, https://doi.org/10.1007/s00703-011-0142-z.

Knuteson, R. O., and Coauthors, 2004: Atmospheric Emitted Radiance Interferometer. Part II: Instrument Performance. *J. Atmos. Ocean. Technol.*, **21**, 1777–1789, https://doi.org/10.1175/JTECH-1663.1.

Kobayashi, H., D. D. Baldocchi, Y. Ryu, Q. Chen, S. Ma, J. L. Osuna, and S. L. Ustin, 2012: Modeling energy and carbon fluxes in a heterogeneous oak woodland: A three-dimensional approach. *Agric. For. Meteor.*, **152**, 83–100, https://doi.org/10.1016/j.agrformet.2011.09.008.

1027 Launiainen, S., and Coauthors, 2016: Do the energy fluxes and surface conductance of boreal
1028 coniferous forests in Europe scale with leaf area? *Glob. Chang. Biol.*, **22**, 4096–4113,
1029 https://doi.org/10.1111/gcb.13497.

1030 Lee, T. R., M. Buban, E. Dumas, and C. B. Baker, 2017: A New Technique to Estimate Sensible
1031 Heat Fluxes around Micrometeorological Towers Using Small Unmanned Aircraft Systems.
1032 *J. Atmos. Ocean. Technol.*, **34**, 2103–2112, https://doi.org/10.1175/JTECH-D-17-0065.1.

1033 ——, ——, ——, and ——, 2019: On the use of rotary-wing aircraft to sample near-surface
1034 thermodynamic fields: results from recent field campaigns. *Sensors*, 19 (1), 10,
1035 https://doi.org/10.3390/s19010010.

1036 Leuning, R., E. van Gorsel, W. J. Massman, and P. R. Isaac, 2012: Reflections on the surface
1037 energy imbalance problem. *Agric. For. Meteor.*, **156**, 65–74,
1038 https://doi.org/https://doi.org/10.1016/j.agrformet.2011.12.002.

1039 Liu, S., and Coauthors, 2016: Upscaling evapotranspiration measurements from multi-site to the
1040 satellite pixel scale over heterogeneous land surfaces. *Agric. For. Meteor.*, **230**–**231**, 97–
1041 113, https://doi.org/https://doi.org/10.1016/j.agrformet.2016.04.008.

1042 Liu, S. M., Z. W. Xu, W. Z. Wang, Z. Z. Jia, M. J. Zhu, J. Bai, and J. M. Wang, 2011: A
1043 comparison of eddy-covariance and large aperture scintillometer measurements with respect
1044 to the energy balance closure problem. *Hydrol. Earth Syst. Sci.*, **15**, 1291–1306,
1045 https://doi.org/10.5194/hess-15-1291-2011.

1046 Löhnert, U., D. D. Turner, and S. Crewell, 2009: Ground-Based Temperature and Humidity
1047 Profiling Using Spectral Infrared and Microwave Observations. Part I: Simulated Retrieval
1048 Performance in Clear-Sky Conditions. *J. Appl. Meteor. Climatol.*, **48**, 1017–1032,
1049 https://doi.org/10.1175/2008JAMC2060.1.

1050 Long, C. N., and T. P. Ackerman, 2000: Identification of clear skies from broadband
1051 pyranometer measurements and calculation of downwelling shortwave cloud effects. *J.*
1052 *Geophys. Res. Atmos.*, **105**, 15609–15626, https://doi.org/10.1029/2000JD900077.

1053 Long, C. N., and Y. Shi, 2008: An Automated Quality Assessment and Control Algorithm for
1054 Surface Radiation Measurements. *Open Atmos. Sci. J.*, **2**, 23–37,
1055 https://doi.org/10.2174/1874282300802010023.

1056 ——, and D. D. Turner, 2008: A method for continuous estimation of clear-sky downwelling
1057 longwave radiative flux developed using ARM surface measurements. *J. Geophys. Res.*,
1058 **113**, D18206, https://doi.org/10.1029/2008JD009936.

1059 ——, T. P. Ackerman, K. L. Gaustad, and J. N. S. Cole, 2006: Estimation of fractional sky cover
1060 from broadband shortwave radiometer measurements. *J. Geophys. Res.*, **111**, D11204,
1061 https://doi.org/10.1029/2005JD006475.

1062 Mahrt, L., 2000: Surface Heterogeneity and Vertical Structure of the Boundary Layer. *Bound.-*
1063 *Layer Meteor.*, **96**, 33–62.

1064 Maronga, B., and Coauthors, 2015: The Parallelized Large-Eddy Simulation Model (PALM)

version 4.0 for atmospheric and oceanic flows: model formulation, recent developments, and future perspectives. *Geosci. Model Dev.*, **8**, 2515–2551, https://doi.org/10.5194/gmd-8-2515-2015.

Maronga, B., and Coauthors, 2020: Overview of the PALM model system 6.0. *Geosci. Model Dev.*, **13**, 1335–1372, https://doi.org/10.5194/gmd-13-1335-2020.

Mauder, M., R. L. Desjardins, and I. Macpherson, 2007a: Scale analysis of airborne flux measurements over heterogeneous terrain in a boreal ecosystem. *J. Geophys. Res.*, **112**, D13112, https://doi.org/10.1029/2006JD008133.

Mauder, M., O. O. Jegede, E. C. Okogbue, F. Wimmer, and T. Foken, 2007b: Surface energy balance measurements at a tropical site in West Africa during the transition from dry to wet season. *Theor. Appl. Climatol.*, **89**, 171–183, https://doi.org/10.1007/s00704-006-0252-6.

Mauder, M., R. L. Desjardins, and I. Macpherson, 2008a: Creating Surface Flux Maps from Airborne Measurements: Application to the Mackenzie Area GEWEX Study MAGS 1999. *Bound.-Layer Meteor.*, **129**, 431–450, https://doi.org/10.1007/s10546-008-9326-6.

Mauder, M., R. L. Desjardins, E. Pattey, Z. Gao, and R. van Haarlem, 2008b: Measurement of the Sensible Eddy Heat Flux Based on Spatial Averaging of Continuous Ground-Based Observations. *Bound.-Layer Meteor.*, **128**, 151–172, https://doi.org/10.1007/s10546-008-9279-9.

Mcgloin, R., L. Šigut, K. Havránková, J. Dušek, M. Pavelka, and P. Sedlák, 2018: Energy balance closure at a variety of ecosystems in Central Europe with contrasting topographies. *Agric. For. Meteor.*, **248**, 418–431, https://doi.org/10.1016/j.agrformet.2017.10.003.

Metzger, S., Durden, D., Paleri, S., Sühring, M., Butterworth, B., Desai, A., Florian, C., Mauder, M., Wanner, L., and Xu, K.: Numerical experiment design doubles scientific return of surface-atmosphere synthesis, in preparation.

Metzger, S., 2018: Surface-atmosphere exchange in a box: Making the control volume a suitable representation for in-situ observations. *Agric. For. Meteor.*, **255**, 68–80, https://doi.org/10.1016/j.agrformet.2017.08.037.

Metzger, S., and Coauthors, 2013: Spatially explicit regionalization of airborne flux measurements using environmental response functions. *Biogeosciences*, **10**, 2193–2217, https://doi.org/10.5194/bg-10-2193-2013.

Nakai, T., H. Iwata, Y. Harazono, and M. Ueyama, 2014: An inter-comparison between Gill and Campbell sonic anemometers. *Agric. For. Meteor.*, **195**–**196**, 123–131, https://doi.org/10.1016/j.agrformet.2014.05.005.

Newman, A. J., P. A. Kucera, and L. F. Bliven, 2009: Presenting the Snowflake Video Imager (SVI). *J. Atmos. Ocean. Technol.*, **26**, 167–179, https://doi.org/10.1175/2008JTECHA1148.1.

Niinemets, Ü., 2001: Global-scale Climatic Controls of Leaf Dry Mass per Area, Density, and Thickness in Trees and Shrubs. Ecology, 82, 453–469, https://doi.org/10.1890/0012-

9658(2001)082[0453:GSCCOL]2.0.CO;2.

Niple, E. R., H. E. Scott, J. A. Conant, S. H. Jones, F. J. Iannarilli, and W. E. Pereira, 2016: Application of oxygen A-band equivalent width to disambiguate downwelling radiances for cloud optical depth measurement. *Atmos. Meas. Tech.*, **9**, 4167–4179, https://doi.org/10.5194/amt-9-4167-2016.

Novak, G. A., M. P. Vermeuel, and T. H. Bertram, 2020: Simultaneous detection of ozone and nitrogen dioxide by oxygen anion chemical ionization mass spectrometry: a fast-time-response sensor suitable for eddy covariance measurements. *Atmos. Meas. Tech.*, **13**, 1887–1907, https://doi.org/10.5194/amt-13-1887-2020.

Oncley, S. P., and Coauthors, 2007: The Energy Balance Experiment EBEX-2000. Part I: overview and energy balance. *Bound.-Layer Meteor.*, **123**, 1–28, https://doi.org/10.1007/s10546-007-9161-1.

Peters, G., B. Fischer, and T. Andersson, 2002: Rain observations with a vertically looking Micro Rain Radar (MRR). Boreal Environ. Res., **7**, 353–362, http://www.borenv.net/BER/pdfs/ber7/ber7-353.pdf.

Pettersen, C., M. S. Kulie, L. F. Bliven, A. J. Merrelli, W. A. Petersen, T. J. Wagner, D. B. Wolff, and N. B. Wood, 2020a: A Composite Analysis of Snowfall Modes from Four Winter Seasons in Marquette, Michigan. *J. Appl. Meteor. Climatol.*, **59**, 103–124, https://doi.org/10.1175/JAMC-D-19-0099.1.

Pettersen, C.; Bliven, L.F.; von Lerber, A.; Wood, N.B.; Kulie, M.S.; Mateling, M.E.; Moisseev, D.M.; Munchak, S.J.; Petersen, W.A.; Wolff, D.B., 2020b: Introducing the Precipitation Imaging Package: Assessment of microphysical and bulk characteristics of snow. Atmosphere, in review.

Pielke, R. A., Sr, R. Avissar, M. Raupach, A. J. Dolman, X. Zeng, and A. S. Denning, 1998: Interactions between the atmosphere and terrestrial ecosystems: influence on weather and climate. *Glob. Chang. Biol.*, **4**, 461–475, https://doi.org/doi:10.1046/j.1365-2486.1998.t01-1-00176.x.

Platis, A., A. F. Moene, D. M. Villagrasa, F. Beyrich, D. Tupman, and J. Bange, 2017: Observations of the Temperature and Humidity Structure Parameter Over Heterogeneous Terrain by Airborne Measurements During the LITFASS-2003 Campaign. *Bound.-Layer Meteor.*, **165**, 447–473, https://doi.org/10.1007/s10546-017-0290-x.

Poulos, G. S., and Coauthors, 2002: CASES-99: A Comprehensive Investigation of the Stable Nocturnal Boundary Layer. *Bull. Amer. Meteor. Soc.*, **83**, 555–581, https://doi.org/10.1175/1520-0477(2002)083<0555:CACIOT>2.3.CO;2.

Raasch, S., and M. Schröter, 2001: PALM - A large-eddy simulation model performing on massively parallel computers. *Meteor. Zeitschrift*, **10**, 363–372, https://doi.org/10.1127/0941-2948/2001/0010-0363.

Ran, Y., X. Li, R. Sun, N. Kljun, L. Zhang, X. Wang, and G. Zhu, 2016: Spatial representativeness and uncertainty of eddy covariance carbon flux measurements for upscaling net ecosystem productivity to the grid scale. *Agric. For. Meteor.*, **230**–**231**, 114–127, https://doi.org/https://doi.org/10.1016/j.agrformet.2016.05.008.

Raupach, M. R., and J. J. Finnigan, 1995: Scale issues in boundary-layer meteorology: Surface energy balances in heterogeneous terrain. *Hydrol. Process.*, **9**, 589–612, https://doi.org/doi:10.1002/hyp.3360090509.

Reen, B. P., D. R. Stauffer, and K. J. Davis, 2014: Land-Surface Heterogeneity Effects in the Planetary Boundary Layer. *Bound.-Layer Meteor.*, **150**, 1–31, https://doi.org/10.1007/s10546-013-9860-8.

Reichstein, M., G. Camps-Valls, B. Stevens, M. Jung, J. Denzler, N. Carvalhais, and Prabhat, 2019: Deep learning and process understanding for data-driven Earth system science. *Nature*, **566**, 195–204, https://doi.org/10.1038/s41586-019-0912-1.

Rihani, J. F., F. K. Chow, and R. M. Maxwell, 2015: Isolating effects of terrain and soil moisture heterogeneity on the atmospheric boundary layer: Idealized simulations to diagnose land-atmosphere feedbacks. *J. Adv. Model. Earth Syst.*, **7**, 915–937, https://doi.org/10.1002/2014MS000371.Received.

Sellers, P., and Coauthors, 1995: The Boreal Ecosystem–Atmosphere Study (BOREAS): An Overview and Early Results from the 1994 Field Year. *Bull. Amer. Meteor. Soc.*, **76**, 1549–1577, https://doi.org/10.1175/1520-0477(1995)076<1549:TBESAO>2.0.CO;2.

Serbin, S. P., A. Singh, B. E. McNeil, C. C. Kingdon, and P. A. Townsend, 2014: Spectroscopic determination of leaf morphological and biochemical traits for northern temperate and boreal tree species. *Ecol. Appl.*, **24**, 1651–1669, https://doi.org/10.1890/13-2110.1.

Steinfeld, G., M. O. Letzel, S. Raasch, M. Kanda, and A. Inagaki, 2007: Spatial representativeness of single tower measurements and the imbalance problem with eddy-covariance fluxes: results of a large-eddy simulation study. *Bound.-Layer Meteor.*, **123**, 77–98, https://doi.org/10.1007/s10546-006-9133-x.

——, S. Raasch, and T. Markkanen, 2008: Footprints in Homogeneously and Heterogeneously Driven Boundary Layers Derived from a Lagrangian Stochastic Particle Model Embedded into Large-Eddy Simulation. *Bound.-Layer Meteor.*, **129**, 225–248, https://doi.org/10.1007/s10546-008-9317-7.

Stoy, P. C., and Coauthors, 2013: A data-driven analysis of energy balance closure across FLUXNET research sites: The role of landscape scale heterogeneity. *Agric. For. Meteor.*, **171**–**172**, 137–152, https://doi.org/10.1016/j.agrformet.2012.11.004.

Sulman, B. N., A. R. Desai, B. D. Cook, N. Saliendra, and D. S. Mackay, 2009: Contrasting carbon dioxide fluxes between a drying shrub wetland in Northern Wisconsin, USA, and nearby forests. *Biogeosciences*, **6**, 1115–1126, https://doi.org/10.5194/bg-6-1115-2009.

Turner, D. D., and W. G. Blumberg, 2019: Improvements to the AERIoe Thermodynamic Profile Retrieval Algorithm. *IEEE J. Sel. Top. Appl. Earth Obs. Remote Sens.*, **12**, 1339–1354,

https://doi.org/10.1109/JSTARS.2018.2874968.

Turner, D. D., and U. Löhnert, 2014: Information Content and Uncertainties in Thermodynamic Profiles and Liquid Cloud Properties Retrieved from the Ground-Based Atmospheric Emitted Radiance Interferometer (AERI). *J. Appl. Meteor. Climatol.*, **53**, 752–771, https://doi.org/10.1175/JAMC-D-13-0126.1.

Twine, T. E., and Coauthors, 2000: Correcting eddy-covariance flux underestimates over a grassland. *Agric. For. Meteor.*, **103**, 279–300, https://doi.org/https://doi.org/10.1016/S0168-1923(00)00123-4.

Vogelmann, H., Speidel, J., and Perfahl, M.: Laser concept of the mobile ATMONSYS-lidar and its application during CHEESEHEAD, EGU General Assembly 2020, https://doi.org/10.5194/egusphere-egu2020-16517

Wagner, T. J., P. M. Klein, and D. D. Turner, 2019: A New Generation of Ground-Based Mobile Platforms for Active and Passive Profiling of the Boundary Layer. *Bull. Amer. Meteor. Soc.*, **100**, 137–153, https://doi.org/10.1175/BAMS-D-17-0165.1.

Wang, J., J. Zhuang, W. Wang, S. Liu, and Z. Xu, 2015: Assessment of Uncertainties in Eddy Covariance Flux Measurement Based on Intensive Flux Matrix of HiWATER-MUSOEXE. *IEEE Geosci. Remote Sens. Lett.*, **12**, 259–263, https://doi.org/10.1109/LGRS.2014.2334703.

Wang, Y. Q., Y. J. Xiong, G. Y. Qiu, and Q. T. Zhang, 2016: Is scale really a challenge in evapotranspiration estimation? A multi-scale study in the Heihe oasis using thermal remote sensing and the three-temperature model. *Agric. For. Meteor.*, **230**–**231**, 128–141, https://doi.org/https://doi.org/10.1016/j.agrformet.2016.03.012.

Wang, Z.**,** P. Wechsler, W. Kuestner, J. French, A. Rodi, B. Glover, M. Burkhart, and D. Lukens, 2009: Wyoming Cloud Lidar: instrument description and applications, *Optics Express* Vol. 17, Iss. 16, pp. 13576–13587.

Wang, Z., A. Chlus, R. Geygan, Z. Ye, T. Zheng, A. Singh, J.J. Couture, J. Cavender-Bares, E.L. Kruger and P.A. Townsend, accepted: Foliar functional traits from imaging spectroscopy across biomes in eastern North America. *New Phytol*.

Wisconsin Department of Natural Resources. (2019). Wisconsin Wiscland 2 Land Cover Database Level 4, 2019. Retrieved from https://data-wi-dnr.opendata.arcgis.com

Wolf, B., and Coauthors, 2017: The SCALEX Campaign: Scale-Crossing Land Surface and Boundary Layer Processes in the TERENO-preAlpine Observatory. *Bull. Amer. Meteor. Soc.*, **98**, 1217–1234, https://doi.org/10.1175/BAMS-D-15-00277.1.

Wu, D., Z. Wang, P. Wechsler, N. Mahon, M. Deng, B. Glover, M. Burkhart, W. Kuestner, and B. Heesen, 2016: Airborne compact rotational Raman lidar for temperature measurement, *Opt. Express*, **24**, A1210-A1223.

Wu, P., H. Shen, T. Ai, and Y. Liu, 2013: Land-surface temperature retrieval at high spatial and

temporal resolutions based on multi-sensor fusion. *Int. J. Digit. Earth*, **6**, 113–133, https://doi.org/10.1080/17538947.2013.783131.

Wulfmeyer, V., S. K. Muppa, A. Behrendt, E. Hammann, F. Späth, Z. Sorbjan, D. D. Turner, and R. M. Hardesty, 2016: Determination of Convective Boundary Layer Entrainment Fluxes, Dissipation Rates, and the Molecular Destruction of Variances: Theoretical Description and a Strategy for Its Confirmation with a Novel Lidar System Synergy. *J. Atmos. Sci.*, **73**, 667–692, https://doi.org/10.1175/JAS-D-14-0392.1.

Wulfmeyer, V., and Coauthors, 2018: A New Research Approach for Observing and Characterizing Land–Atmosphere Feedback. *Bull. Amer. Meteor. Soc.*, **99**, 1639–1667, https://doi.org/10.1175/BAMS-D-17-0009.1.

Xu, K., S. Metzger, and A. R. Desai, 2017a: Upscaling tower-observed turbulent exchange at fine spatio-temporal resolution using environmental response functions. *Agric. For. Meteor.*, **232**, 10–22, https://doi.org/10.1016/j.agrformet.2016.07.019.

——, ——, and A. R. Desai, 2018: Surface-atmosphere exchange in a box: Space-time resolved storage and net vertical fluxes from tower-based eddy covariance. *Agric. For. Meteor.*, **255**, 81–91, https://doi.org/10.1016/j.agrformet.2017.10.011.

Xu, Z., Y. Ma, S. Liu, W. Shi, and J. Wang, 2017b: Assessment of the Energy Balance Closure under Advective Conditions and Its Impact Using Remote Sensing Data. *J. Appl. Meteor. Climatol.*, **56**, 127–140, https://doi.org/10.1175/JAMC-D-16-0096.1.

Xu, K., M. Sühring, S. Metzger, D. Durden, and A. R. Desai, 2020: Can Data Mining Help Eddy Covariance See the Landscape? A Large-Eddy Simulation Study. *Bound.-Layer Meteor.*, **176**, 85–103, https://doi.org/10.1007/s10546-020-00513-0.

Zhu, X., G. Ni, Z. Cong, T. Sun, and D. Li, 2016: Impacts of surface heterogeneity on dry planetary boundary layers in an urban-rural setting. *J. Geophys. Res. Atmos.*, **121**, 164–179, https://doi.org/10.1002/2016JD024982.

Zitouna-Chebbi, R., L. Prévot, F. Jacob, R. Mougou, and M. Voltz, 2012: Assessing the consistency of eddy covariance measurements under conditions of sloping topography within a hilly agricultural catchment. *Agric. For. Meteor.*, **164**, 123–135, https://doi.org/10.1016/j.agrformet.2012.05.010.

SUPPLEMENTAL MATERIAL

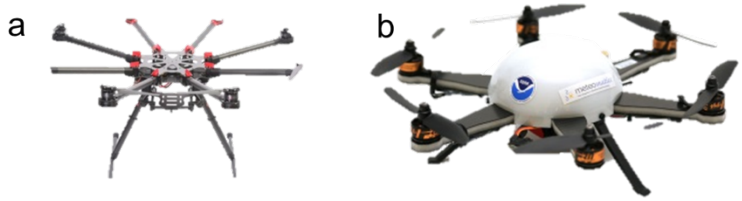

Fig. S1. The (a) DJI S-1000 and (b) Meteodrone SSE.

Table S1. List of the flux towers in operation during the CHEESEHEAD19 field campaign.

Site #	Site Name	Ameriflux ID	Latitude (° N)	Longitude (° W)	Tower height (m)	Canopy height (m)	Vegetation	Contact
1	NW1	US-PFb	45.97200	90.32317	32	25	pine	Oncley
2	NW2	US-PFc	45.96773	90.30878	12	3	aspen	Oncley
3	NW3	US-PFd	45.96892	90.30103	3	0.3	wetland	Oncley
4	NW4	US-PFe	45.97925	90.30042	32	20.1	lake	Oncley
5	NW5	US-PFf	45.94583	90.29437	2	0	grass	Stoy
6	NE1	US-PFg	45.97348	90.27230	32	33.2	pine	Oncley
7	NE2	US-PFh	45.95573	90.24060	32	19.2	pine	Oncley
8	NE3	US-PFi	45.97490	90.23273	32	18.3	hardwood	Oncley
9	NE4	US-PFj	45.96187	90.22703	32	18.3	maple	Oncley
10	SW1	US-PFk	45.91490	90.34250	32	24.4	aspen	Oncley
11	SW2	US-PFl	45.94090	90.31773	25	19.2	aspen	Oncley
12	SW3	US-PFm	45.92067	90.30990	32	15	hardwood	Oncley
13	SW4	US-PFn	45.93922	90.28232	32	25.9	hardwood	Oncley
14	SE1	US-PFo	45.92288	90.27283	1.5	0	lake	Stoy
15	SE2	US-PFp	45.93652	90.26408	32	24.4	hardwood	Oncley
16	SE3	US-PFq	45.92715	90.24750	32	14.3	aspen	Oncley
17	SE4	US-PFr	45.92448	90.24745	3	0.3	wetland	Oncley
18	SE5	US-PFs	45.93808	90.23818	12	3.1	aspen	Oncley
19	SE6	US-PFt	45.91973	90.22883	32	21.6	pine	Oncley
20	WLEF	US-PFa	45.94590	90.27230	396	n/a	mixed	Desai
21	WCR	US-WCr	45.80600	90.07980	30	24	hardwood	Desai
22	LOS	US-Los	46.08270	89.97920	10	2	wetland	Desai

Table S2. Instrumentation deployed at the CHEESEHEAD19 campaign by the NOAA Global Monitoring Laboratory

Instrument	Measurement	Dates (2019)	Resolution
Central ISS Station			
Eppley Pyrgeometer	⇵ LW broadband hemispheric irradiance	06/29 - 10/22	1 min avg.
Eppley Precision Spectral Pyranometer (PSP)	⇵ SW broadband hemispheric irradiance	06/29 - 10/22	1 min avg.
Shaded Eppley Black and White Pyranometer	Diffuse hemispheric broadband SW irradiance	06/29 - 10/22	1 min avg.
Eppley Normal Incidence Pyrheliometer (NIP)	Direct normal broadband SW irradiance	06/29 - 10/22	1 min avg.
Total Sky Imager (TSI)	Images/movies of sky cover, fractional sky cover	07/05 - 10/22	15 sec
Vaisala CL51 Ceilometer	Cloud base height, boundary layer height	06/29 - 10/22	16 sec
Multi Filter Rotating Shadowband Radiometer (MFRSR)	↓ hemispheric total and diffuse spectral irradiance at 6 bands: 415, 500, 670, 868, 940, 1625 nm; retrievals of aerosol optical depth	06/29 - 10/22	20 sec
Multi Filter Radiometer (MFR)	↑ hemispheric total spectral irradiance at 6 bands: 415, 500, 670, 868, 940, 1625 nm. Spectral surface albedo and NDVI (with MFRSR).	06/29 - 10/22	20 sec
LICOR Quantum 190R	Photosynthetically Active Radiation	06/29 - 10/22	1 min avg.
Aerodyne Three-Waveband Spectrally-agile Technique (TWST)	Cloud optical depth, spectral SW zenith radiance (350-1000 nm, ~2.5 nm resolution)	09/20 - 10/22	1 sec
Vaisala HMP60	Temperature and Relative Humidity	06/29 - 10/22	1 min avg.
RM Young, Model 05103	Wind direction and speed at 10 m	06/29 - 10/22	1 min avg.
Prentice and Lakeland Airports			
Eppley Pyrgeometer	↓ LW broadband hemispheric irradiance	06/28 - 10/23	1 min avg.
Kipp & Zonen CMP11 Pyranometer	↓ SW broadband hemispheric irradiance	06/28 - 10/23	1 min avg.
Delta-T SPN-1 Radiometer	↓ SW diffuse and total broadband hemispheric irradiance	06/28 - 10/23	1 min avg.
Vaisala HMP60	Temperature and Relative Humidity	06/28 - 10/23	1 min avg.
Vaisala CL-51 Ceilometer	Cloud Base Height (CBH)	06/28 - 10/23	16 sec

1258
1259

Table S3. The dates, times, and flight patterns of the UWKA flights.

Date	Flight Number	Takeoff (UTC)	Landing (UTC)	Entered Domain (UTC)	Exited Domain (UTC)	Flight Pattern
7/9/19	RF01	13:57	16:47	14:06	16:16	WE2
7/9/19	RF02	19:02	21:32	19:11	21:22	WE2
7/11/19	RF03	14:10	17:00	14:22	16:36	WE1
7/11/19	RF04	19:00	21:40	19:15	21:28	WE1
7/12/19	RF05	13:40	16:45	13:49	16:06	WE2
7/12/19	RF06	17:52	21:00	18:04	20:46	WE2
7/13/19	RF07	14:05	16:52	14:22	16:32	SE2
7/13/19	RF08	18:56	21:30	19:12	21:16	SW1
8/20/19	RF09	13:40	16:23	13:51	16:12	SE1
8/20/19	RF10	19:12	22:22	19:23	21:51	SE1
8/21/19	RF11	13:54	16:50	14:08	16:36	SW1
8/21/19	RF12	18:55	21:50	19:11	21:38	SW1
8/22/19	RF13	13:57	17:15	14:11	16:55	SW2
8/22/19	RF14	19:00	22:01	19:13	21:46	SW2
8/23/19	RF15	13:57	16:48	14:07	16:38	WE2
8/23/19	RF16	19:07	22:03	19:17	21:46	WE2
9/24/19	RF17	13:37	17:00	13:53	16:24	SE1
9/24/19	RF18	18:57	21:49	19:10	21:39	SE1
9/25/19	RF19	14:20	17:22	14:41	17:09	SW1
9/25/19	RF20	19:12	22:06	19:29	21:53	SW1
9/26/19	RF21	13:52	16:46	14:05	16:35	SE1
9/26/19	RF22	18:31	21:40	18:45	21:14	SE1
9/28/19	RF23	14:14	17:30	14:37	17:17	WE1
9/28/19	RF24	18:50	21:50	19:07	21:36	WE1

1260
1261

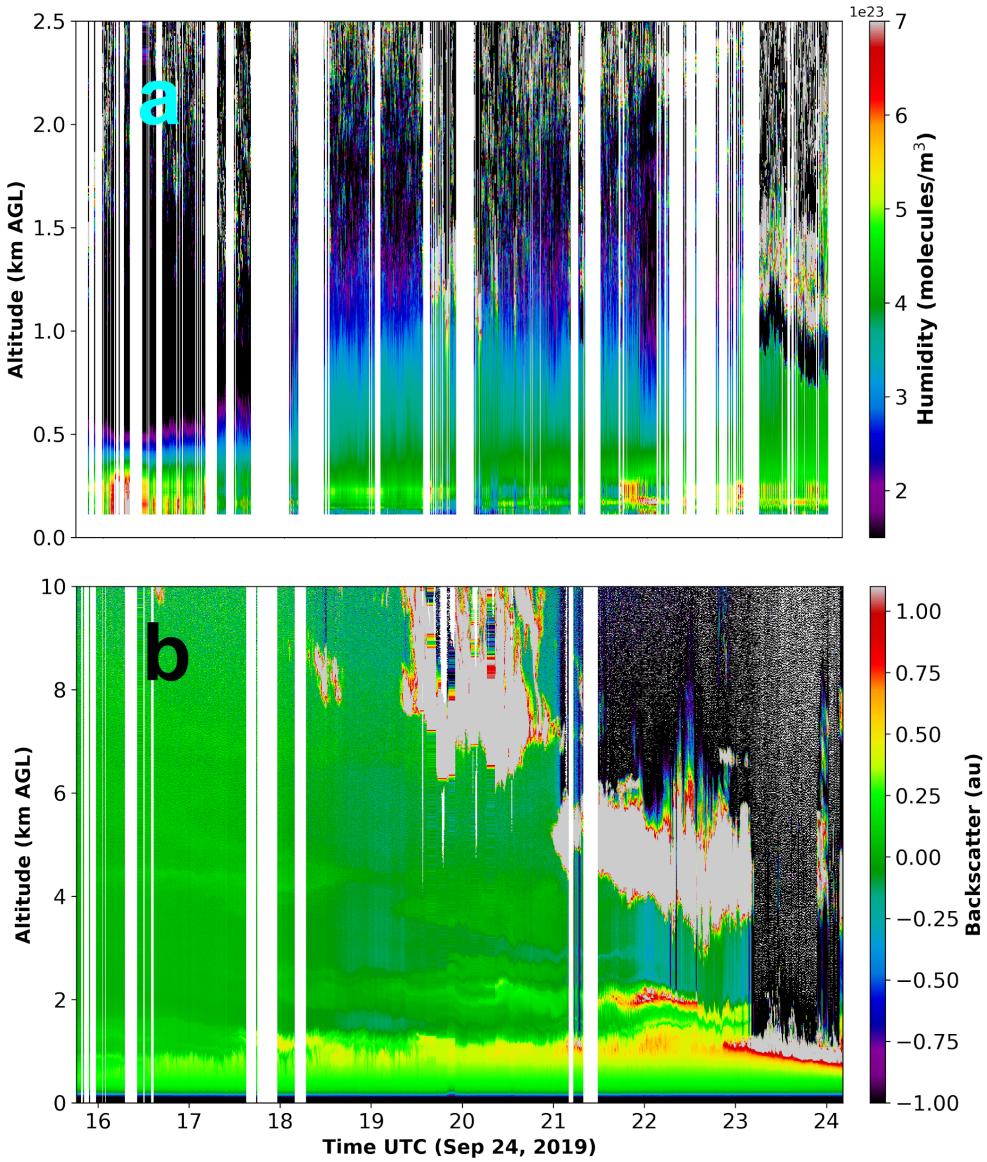

Fig S2. Preliminary profiles of (a) H_2O and (b) backscatter measured by the ATMONSYS lidar. These are complementary, collocated datasets with the HSRL, AERI, and MWR at WLEF. The high resolution data (vertical resolution of 110 m and 7.5 m for H_2O and backscatter, respectively; 20 second temporal resolution for both) are capable of being combined with collocated Doppler wind lidar data to calculate flux profiles.

ACKNOWLEDGEMENTS

We thank the many groups and individuals whose contributions made this project possible. From the US Forest Service we thank Linda Parker, Melanie Fullman, Jonathan McNeill, and Jim Mineau. We thank Linda Cully at NCAR EOL for creating the project web page and data repository. Thank you to the colleagues who helped deploy the NOAA instruments: Ed Dumas,

Gary Hodges, Emiel Hall, Christian Herrera, Hagen Telg, Jim Wendell, Herman Scott, Irina Djalalova, Laura Bianco, Tom Ayers, Matt Carney, Doug Kennedy, Sean Waugh, Petra Klein, and Tyler Bell. Thank you to the UWKA support crew: Matt Burkhart, Min Deng, Tom Drew, Brent Glover, Zane Little, Austin Morgan, Larry Oolman, Ed Sigel, and Brett Wadsworth. We thank the UW administrative, communications, and technical support from Wayne Feltz, Brad Pierce, Jenny Hackel, Chelsea Dahmen, Christi Levenson, Sue Foldy, Bailey Murphy, Leo Mikula, Ryan Clare, Kelly Tyrell, and Jeff Miller. Thank you to the team from UW-Madison FWE who assisted in the field work, processing, and administrative activities, including Jacob May in lidar drone deployment, field sampling by Ella Norris, Ben Sellers, Sam Jaeger, Nanfeng Liu, Ben Spaier, Josh Phillips; and airborne data collection and processing Erin Hokanson Wagner, Brendan Heberlein, and Nanfeng Liu. Thank you to Karla Ortman and Scott Bowe at Kemp Natural Resources Station for assisting with lodging needs of the project. We appreciate the on-going support of Jeff Ayers, Steve Bauder, Jeff Ohnstad, Doug Siroin, and Marta Bechtol of the Wisconsin Educational Communication Board who own and operate the WLEF tall tower. Thank you to Noah R. Lottig, Paul Schram, and Emily Stanley of the UW Center for Limnology for providing equipment and processing water pCO_2 samples. Thank you to Matthias Perfahl of KIT for technical operation of the ATMONSYS lidar, Gabe Bromley for EC installation, and Ke Xu for project lead-up research. Thank you to UW-Eau Claire students Josie Radtke and Whitney Mottishaw for technical support. We also thank those involved in the UW-Madison AOS404 class: Susi Weisner, Jess Turner, Sophie Hoffman, Juliet Pilewskie, Iman Nasif, Peter Janssen, as well as April Hiscox and the U South Carolina class. Thank you to Laurie Fox and the students at Butternut School and Travis Augustine and the students at Chequamegon High School Class ACT charter who helped collect data. We acknowledge Christopher Bosma, who helped deploy the MRRPro. Thank you to Tania Kleynhans and Aaron Gerace for processing Landsat 8 LST data. Thank you to the NOAA Carbon Cycle and Greenhouse Gas group: Arlyn Andrews, Jonathan Kofler, Colm Sweeney, and Issac Vimont. Thank you to the group operating TCCON: Paul Wennberg and Debra Wunch. Thank you to the team from NASA: Joel McCorkel, Eric Vermote, and Bill Rountree. We thank Ann Wojcieszak for allowing instruments to be installed on her property (the ISS field). We thank Brittany Bloodhart, Emily Fischer, Erika Marin-Spiotta for organizing the fieldwork surveys and bullying and sexual harassment prevention training. Lastly, we thank our friends at Park Falls Gastropub - the official pub of the CHEESEHEAD19 project.